Graft-Induced Reprogramming Under Arterial Hemodynamic Stress is Associated with a Shared Proteomic Phenotype in Arterial and Venous Conduits Following Coronary Artery Bypass Grafting

Eun Na Kim, MD.PhD.[1†], Suk Ho Sohn, MD.PhD.[2†], Jiyoung Yu, PhD.[3†], Joon Seo Lim, PhD.[4], Jiwon Koh, MD.PhD.[1], Jaemoon Koh, MD.PhD.[1], Changha Hwang, PhD.[5,6], Kyunggon Kim, PhD.[7‡], Ho Young Hwang, MD.PhD.[2‡], Se Jin Oh, MD.PhD.[8‡]

[1]Department of Pathology, Seoul National University Hospital, Seoul National University College of Medicine, Seoul, Republic of Korea

[2]Department of Thoracic and Cardiovascular Surgery, Seoul National University Hospital, Seoul National University College of Medicine, Seoul, Republic of Korea

[3]Clinical Proteomics Core Lab, Convergence Research Center, Asan Medical Center, Seoul, Republic of Korea

[4]Clinical Research Center, Asan Medical Center, University of Ulsan College of Medicine, Seoul, Republic of Korea

[5]Department of Applied Statistics, Dankook University, Gyeonggi-do, Republic of Korea

[6]Arontier, Seoul, Republic of Korea

[7]Department of Digital Medicine, BK21 Project, Asan Medical Center, University of Ulsan College of Medicine, Seoul, Republic of Korea

[8]Department of Thoracic and Cardiovascular Surgery, SMG-SNU Boramae Medical Center, Seoul National University College of Medicine, Seoul, Republic of Korea

SHORT TITLE: Proteomic Convergence of Arterial/Venous Grafts

[†]These authors have contributed equally to this work and share the first authorship

[‡]These authors have contributed equally to this work and share the corresponding authorship

CORRESPONDING AUTHORS

Kyunggon Kim, PhD

Department of Digital Medicine, BK21 Project

Asan Medical Center, University of Ulsan College of Medicine

88, Olympic-ro 43-gil, Songpa-gu, Seoul 05505, Republic of Korea

Email: kimkyunggon@gmail.com

Ho Young Hwang, MD, PhD

Department of Thoracic and Cardiovascular Surgery

Seoul National University Hospital, Seoul National University College of Medicine

101 Daehak-ro, Jongno-gu, Seoul 03080, Republic of Korea

Email: scalpel@snu.ac.kr

Se Jin Oh, MD, PhD (Lead contact)

Department of Thoracic and Cardiovascular Surgery

SMG-SNU Boramae Medical Center, Seoul National University College of Medicine

20, Boramae-ro 5-gil, Dongjak-gu, Seoul 07061, Republic of Korea

Email: wpwnn@snu.ac.kr

THE TOTAL WORD COUNT OF THE MANUSCRIPT: 8128

ABSTRACT

Background: Autologous venous conduits remain the mainstay of coronary artery bypass grafting (CABG); however, their long-term patency is limited by adverse vascular remodeling. While arterial and venous grafts undergo structural and molecular adaptation to arterial hemodynamics, the mechanisms underlying successful adaptation remain poorly characterized owing to the scarcity of functioning human graft tissues.

Methods: We analyzed bypass grafts explanted en bloc during orthotopic heart transplantation, comprising patent vein grafts (VGP, n=19), occluded vein grafts (VGO, n=9), and patent arterial grafts (AGP, n=13), alongside freshly harvested controls (vein, n=23; artery, n=11). Quantitative histomorphometry, label-free LC–MS/MS proteomics, pathway analysis, and immunohistochemistry were performed.

Results: While patent arterial and venous grafts exhibited medial elastin reinforcement, adventitial neovascularization, and organized intimal remodeling, occluded vein grafts demonstrated elastic layer disruption, medial degeneration, and collagen-dense fibrosis. Proteomic analysis revealed a convergent adaptive signature in patent grafts enriched for RNA metabolism, protein synthesis, cytoskeletal dynamics, and extracellular matrix organization, with shared activation of NR4A3, STAT1, and EGFR signaling. Vein-specific adaptation involved SRC–PTGES activation with concomitant STAT3 suppression, whereas arterial grafts engaged IGF1–RUNX2-associated proliferative programs. Failed venous grafts exhibited angiotensin-driven fibroinflammatory remodeling. Endothelial nitric oxide synthase expression was markedly upregulated in the luminal endothelium and adventitial neovessels of patent grafts.

Conclusions: Despite distinct vascular origins, arterial and venous grafts converged toward a shared adaptive phenotype characterized by structural maturation and vasoprotective

signaling. Targeting common adaptive pathways—including NR4A3, STAT1, EGFR, and adventitial eNOS—may offer therapeutic strategies to enhance long-term graft durability.

WHAT ARE THE CLINICAL IMPLICATIONS?

This study provides human tissue–based evidence that patent coronary bypass grafts share a common adaptive remodeling program, irrespective of whether the conduit is arterial or venous. Rather than simple venous "arterialization," successful grafts converged on a phenotype characterized by coordinated biosynthetic activity, structural maturation, and vasoprotective signaling, whereas occluded vein grafts exhibited a distinct angiotensin-driven fibroinflammatory remodeling program. Importantly, patent grafts demonstrated conserved upregulation of NR4A3, STAT1, EGFR, and endothelial nitric oxide synthase (eNOS) in both luminal and adventitial endothelial compartments, identifying molecular features that distinguish adaptive from maladaptive remodeling in humans.

These findings are clinically relevant because they highlight shared, potentially targetable pathways that may support graft durability across conduit types and provide mechanistic support for surgical strategies that preserve perivascular adipose tissue during vein harvesting. Moreover, the association of graft failure with angiotensin-centered extracellular matrix remodeling suggests a modifiable biological axis that warrants further investigation. Together, this work establishes a human molecular framework for graft adaptation that may inform future biomarker development, therapeutic targeting, and precision strategies aimed at improving outcomes after coronary artery bypass grafting.

97 **NON-STANDARD ABBREVIATIONS AND ACRONYMS**

AC	Artery control
AGP	Artery graft, patent
CABG	Coronary artery bypass grafting
DAB	3,3′-Diaminobenzidine
ECM	Extracellular matrix
eNOS	Endothelial nitric oxide synthase
FFPE	Formalin-fixed, paraffin-embedded
IGF1	Insulin-like growth factor 1
IPA	Ingenuity Pathway Analysis
LC–MS/MS	Liquid chromatography–tandem mass spectrometry
PCA	Principal component analysis
PGC-1α	Peroxisome proliferator-activated receptor gamma coactivator-1 alpha (PPARGC1A)
PPI	Protein–protein interaction
PVAT	Perivascular adipose tissue
RUNX2	Runt-related transcription factor 2
SRC	Src proto-oncogene, non-receptor tyrosine kinase
SRP	Signal recognition particle
STAT	Signal transducer and activator of transcription
VC	Vein control
VEGF	Vascular endothelial growth factor
VGO	Vein graft, occluded
VGP	Vein graft, patent

98

INTRODUCTION

Coronary artery bypass grafting (CABG) remains a primary revascularization strategy for multivessel coronary artery disease; however, patient outcomes continue to heavily depend on long-term graft performance[1]. Arterial grafts, characterized by their elastic architecture and intrinsic compatibility with the high-pressure coronary circulation, exhibit superior long-term patency[2]. In contrast, venous grafts are abruptly exposed to arterial hemodynamics that differ fundamentally from their low-pressure venous origin and must undergo extensive adaptive remodeling to maintain patency[3]. Although arterial conduits—including the internal mammary artery, radial artery, and other elastic or muscular arteries—provide the most durable options[4], their limited availability and anatomical constraints often necessitate the use of venous grafts in patients with multivessel disease[5]. Consequently, mitigating venous graft failure has become a key determinant of long-term outcomes following CABG.

Failure of this adaptive process—particularly in venous grafts—precipitates early thrombosis, excessive intimal hyperplasia, and accelerated atherosclerosis, events that collectively contribute to their significantly lower patency compared to arterial conduits[6,7]. Because graft failure can result in recurrent ischemia, repeat revascularization, and even sudden cardiac death, elucidating the biological mechanisms that preserve graft integrity is essential for improving CABG outcomes.

Although the mechanisms contributing to venous graft failure have been extensively described, the biological processes that enable successful graft adaptation remain poorly understood. Previous human studies have primarily examined conduits at the time of harvesting[8] or on grafts removed following clinical failure[9], offering limited insight into the structural and molecular changes that occur in vivo during graft function. As a result, the histomorphological features, molecular pathways, and vasoprotective mechanisms that support adaptation to coronary hemodynamic stress remain incompletely characterized.

Recent attention has focused on strategies such as no-touch harvesting and the preservation of perivascular adipose tissue (PVAT), both of which have been associated with improved graft performance[10,11]. Proposed mechanisms include enhanced endothelial integrity and increased endothelial nitric oxide synthase (eNOS) expression in freshly harvested no-touch conduits[12,13]. However, these observations are limited to pre-implant tissue, and direct evidence linking PVAT-associated or endothelial eNOS to graft patency in humans remains lacking.

A further conceptual gap concerns the traditional assumption that venous conduits undergo “arterialization” after implantation[3]. Although this term is widely used to describe the adaptive transition of veins exposed to arterial pressure, the molecular basis, temporal progression, and histomorphological correlates of this process in clinically patent grafts have never been systematically defined. It remains uncertain whether venous conduits undergo a unidirectional transition toward an arterial phenotype while arterial grafts largely preserve their native architecture, or whether more complex adaptive programs are involved.

In this study, we leveraged a rare clinical circumstance that offers uniquely valuable biological insights by enabling the direct examination of both arterial and venous bypass grafts explanted en bloc at the time of orthotopic heart transplantation. Using an integrated approach that combines quantitative histomorphology, high-resolution proteomics, and targeted immunohistochemistry, we examined not only occluded venous grafts but also successfully functioning venous and arterial grafts. By contrasting these specimens, we aimed to define the adaptive remodeling pathways, signaling trajectories, and conduit-specific mechanisms that support graft patency in humans.

149 **METHODS**

150 **Study Approval and Patient Samples**

151 This study was approved by the institutional review boards of Seoul National University
152 Hospital (J-2306-002-1435) and SMG-SNU Boramae Medical Center (10-2023-25) on June
153 2, 2023. Written informed consent was obtained from all participants.

154 A total of eight patients who had previously undergone CABG and subsequently
155 received orthotopic heart transplantation for end-stage heart failure (Figure 1A) were
156 enrolled. Patient demographics are summarized in Table S1. All vein grafts were saphenous
157 vein conduits, and all artery grafts were internal mammary arteries. Accordingly, the terms
158 "vein graft" and "artery graft" were used to refer to these respective conduit types.

159 Seven patients underwent both procedures at Seoul National University Hospital and
160 SMG-SNU Boramae Medical Center and received vein grafts harvested using the no-touch
161 technique, configured in Y- or I-graft arrangements, and anastomosed to the in-situ arterial
162 graft. One patient, who underwent CABG at an external institution, received conventionally
163 harvested vein grafts with aortocoronary anastomosis. Graft patency prior to transplantation
164 was assessed using coronary angiography or multi-detector computed tomography. The
165 median interval from CABG to transplantation was 74 months (range, 0.2–226 months).

166

167 **Histomorphological Analysis**

168 For histological assessment, we analyzed 41 formalin-fixed, paraffin-embedded (FFPE) graft
169 blocks, including 13 artery graft patent (AGP) blocks from 5 patients, 19 vein graft patent
170 (VGP) blocks from 6 patients, and 9 vein graft obstructed (VGO) blocks from 2 patients. As
171 controls, freshly harvested graft tissues were obtained from 28 patients undergoing CABG,
172 yielding 11 artery control (AC) blocks from 11 patients and 23 vein control (VC) blocks from
173 23 patients.

FFPE tissue blocks were sectioned into 4-μm-thick slides and stained with hematoxylin and eosin, elastin, and Masson's trichrome (MT) to evaluate histological features, including elastic fiber content, the formation of internal and external elastic laminae, and intimal fibrosis. Slides were digitized using a whole-slide scanner (Aperio GT450 DX, Leica Biosystems). Manual annotations were performed using QuPath (https://qupath.github.io/), followed by quantification of intima, media, and adventitia thickness and area, as well as luminal, medial, and adventitial circumferences. Additionally, the number and depth of clefts within the hyperplastic intima were quantified (Figure S1).

Details on the methodologies regarding proteomic analysis, LC-MS/MS, database search, canonical pathway analysis, immunohistochemistry, and statistical analysis are provided in **Supplemental Methods**.

RESULTS

Histomorphological Characteristics of Patent Arterial and Venous Grafts

We analyzed 41 FFPE vessel and graft specimens to characterize baseline vascular architecture and graft-associated morphological remodeling (Figure 1B-D). After exposure to arterial hemodynamics, VGP underwent pronounced structural remodeling, characterized by substantial intimal and medial thickening, the development of a well-defined internal elastic lamina, and an increased presence of elastic fibers interwoven within the medial layer. In addition, a newly formed, wavy elastic layer between the media and adventitia was consistently observed, representing a structural reorganization that renders the venous wall similar to the layered organization typical of arterial conduits. In contrast, VGO showed aneurysmal dilatation, loss of organized elastic layers, medial degeneration, and collapse of the normal intima–media–adventitia boundaries, consistent

198 with structural failure rather than adaptive remodeling. Detailed results of quantitative
199 morphometric analysis and intimal measurements are provided in **Supplemental Results**.
200

201 **Immunohistochemical Analysis of Patent and Occluded Vein Grafts**

202 Histochemical and immunohistochemical staining (Figure 1E) revealed distinct differences in
203 intimal organization between patent and occluded vein grafts. In VGP, elastic staining
204 demonstrated a well-organized intima and media. Masson's trichrome staining indicated
205 fibrosis; however, the collagen matrix maintained a structured pattern with interspersed
206 αSMA-positive myofibroblasts, suggesting an orderly and adaptive remodeling process. In
207 contrast, VGO displayed a fundamentally different morphology. Elastic staining revealed
208 significant disruption of the elastic lamina structures. Masson's Trichrome staining
209 demonstrated dense, disorganized collagen consistent with a non-cellular fibrotic matrix, and
210 αSMA staining confirmed the absence of smooth muscle–type cells within the thickened
211 intima.
212

213 **Proteomics**

214 ***Global Proteomic Profiling Reveals Condition-Specific Molecular Signatures***

215 To characterize the molecular landscape of vascular remodeling during graft adaptation
216 and failure, we performed quantitative proteomic analysis using LC-MS/MS on five
217 experimental groups: VC, AC, VGP, AGP, and VGO. A total of 4,836 proteins were
218 identified across all vascular samples (Figure 2A). Unsupervised two-dimensional PCA
219 revealed a clear separation between AC and VC samples. In contrast, AGP and VGP samples
220 clustered closely together. VGO samples formed a distinct, isolated cluster, separate from
221 both native vessels and patent grafts (Figure 2B).
222

223

224 **Volcano Plot Analysis of Graft-Associated Proteomic Changes**

225 Volcano plot analysis (Figure 2C) revealed extensive proteomic remodeling across all graft
226 types. Only a very small subset of proteins differed between AGP and VGP, underscoring the
227 proteomic similarity between the two conduits after grafting. In contrast, the comparison
228 between VGP and VGO showed marked divergence, with 475 proteins enriched in VGP and
229 220 enriched in VGO.

230

231 **Canonical Pathway Enrichment Analysis of AGP and VGP**

232 Canonical pathway enrichment analysis (Figure 2D) demonstrated that AGP (vs. AC) and
233 VGP (vs. VC) share a broad set of commonly enriched pathways. Both comparisons showed
234 significant activation of translation-associated programs, indicating similarities in
235 biosynthetic and proteostasis-related pathways in both graft types.

236

237 **Hierarchical Clustering Revealed Group-Specific Proteomic Signatures**

238 Hierarchical clustering of the 2,492 differentially expressed proteins revealed distinct group-
239 specific expression patterns across vascular samples (Figure 2E)—VC in Cluster 7, AC in
240 Cluster 6, VGO in Cluster 5, and both AGP and VGP in Cluster 4. To further characterize the
241 biological processes represented by each cluster, we employed a three-tiered analytical
242 workflow consisting of: (1) pathway enrichment analysis using Ingenuity Pathway Analysis,
243 which offers a function-centered interpretation of overrepresented biological programs; (2)
244 protein–protein interaction (PPI) network analysis using the STRING database[14], which
245 delineates the structural and functional connectivity among proteins; and (3) integrative
246 functional annotation using the Metascape[15] enrichment bubble plot (GO/KEGG/Reactome).
247 These analyses were conducted on cluster-specific protein subsets derived from the

248 hierarchical clustering: AC (Cluster 6, n=171 proteins), VC (Cluster 7, n=340 proteins), VGP
249 + AGP (Cluster 4, n=741 proteins), and VGO (Cluster 5, n=210 proteins).
250

251 **Integrated Functional Analysis Revealed Fundamentally Distinct Remodeling Programs**
252 **Represented by Clusters 4 and 5**

253 Cluster 4 (VGP + AGP) captured the shared proteomic signature of patent arterial and venous
254 grafts. Pathway enrichment analysis (Figure 3A) demonstrated coordinated activation of
255 RNA metabolism, mRNA processing, translation initiation and elongation, ribonucleoprotein
256 biogenesis, and SRP-dependent cotranslational protein targeting to membranes, along with
257 pathways supporting extracellular matrix (ECM) organization and cytoskeletal adaptation.
258 PPI network analysis (Figure 3B) revealed densely interconnected ribosomal and translation
259 hubs, as well as organized ECM-remodeling subnetworks, consistent with an active,
260 reparative remodeling phenotype. In contrast, Cluster 5 (VGO) represented the molecular
261 landscape of failed vein grafts. Pathway enrichment analysis revealed predominant activation
262 of complement and coagulation cascades, acute inflammatory signaling, wound healing, and
263 disorganized ECM remodeling. PPI networks (Figure S4) formed extensive thrombo-
264 inflammatory modules and collagen-rich ECM clusters, indicating a shift toward a
265 maladaptive, pro-inflammatory, and pro-thrombotic phenotype.

266 Metascape-based functional annotation (Figure 3C) further distinguished the adaptive
267 and maladaptive programs of these clusters. Cluster 4 showed enrichment in RNA
268 metabolism, VEGFA–VEGFR2 signaling, receptor tyrosine kinase pathways, protein
269 maturation, intracellular transport, lysosomal activity, and immune-regulatory processes,
270 reflecting a biosynthetically vigorous, structurally adaptive, and immunologically balanced
271 program characteristic of successful grafts. In contrast, Cluster 5 was enriched in complement
272 and coagulation cascades, NABA matrisome pathways, extracellular matrix organization,

273 platelet activation, plasma lipoprotein assembly, and IGFBP-mediated IGF transport
274 regulation. This enrichment is consistent with a matrix-disruptive, thrombosis-prone, and
275 growth factor–dysregulated environment associated with graft obstruction.
276 Canonical pathway analysis further revealed distinct activation patterns across graft
277 conditions, with biosynthetic and vascular remodeling pathways predominating in functional
278 grafts, while inflammatory and coagulative pathways characterized occluded grafts.
279

280 **Activation of Proliferative and Biosynthetic Programs and Suppression of Contractile**
281 **Regulators in Patent Grafts**

282 Upstream regulator analysis of patent grafts compared to native vessels revealed coordinated
283 activation of proliferative and biosynthetic signaling networks. In AGP, key activated
284 upstream nodes included IGF1, RUNX2, NR4A3, PGC-1α, EGFR, and MYC (Figure 4A). In
285 VGP, STAT1, SRC, PTGES, resistin (RETN), and G6PD were identified as activated nodes,
286 forming a coherent regulatory network (Figure 4A,B). In contrast, regulators involved in
287 vascular contractility and cytoskeletal integrity, including serum response factor (SRF) and
288 myocardin-related transcription factor A (MRTFA), were predicted to be inhibited in VGP.
289 This transcriptional profile indicates phenotypic modulation toward a synthetic phenotype,
290 characterized by enhanced extracellular matrix production, increased biosynthetic capacity,
291 and elevated proliferative activity—hallmarks of adaptive vascular remodeling during vein
292 graft transformation in the arterial circulation.
293

294 **Immunohistochemical Validation of Key Regulatory Nodes**

295 To validate pathway-level predictions, immunohistochemical analysis was performed on key
296 upstream regulators identified through IPA analysis (Figure 4C). Shared adaptive regulators
297 across both graft types—NR4A3, EGFR, and STAT1—demonstrated significantly increased

298 expression in both arterial grafts (AGP vs. AC, P<0.01) and venous grafts (VGP vs. VC,
299 P<0.01), establishing these as conserved adaptive regulators during adaptation to arterial
300 hemodynamics. Notably, the expressions of NR4A3 and EGFR were markedly reduced in
301 VGO, consistent with regression of proliferative signaling during graft failure. Graft-Type–
302 Specific Adaptive Signatures AGP exhibited significant increases in IGF1 and RUNX2
303 expression compared to native AC, validating pathway predictions of growth factor–driven
304 proliferative and osteogenic signaling in arterial graft adaptation. Conversely, VGP showed
305 elevated expression of RETN (resistin), SRC, and PTGES compared to native VC,
306 confirming graft-type–specific activation of metabolic stress and biosynthetic mediator
307 pathways predicted by IPA analysis.
308 PGC-1α—a factor predicted by the proteomic model to vary by graft type—showed an
309 upward trend in both arterial and venous grafts (AGP > AC; VGP > VC), although the
310 differences did not reach statistical significance (AC vs. AGP, P=0.177; VC vs. VGP,
311 P=0.104). Similarly, c-Myc expression tended to be higher in AGP compared with AC, but
312 this difference was not statistically significant (P=0.114) (Figure S14).
313 Collectively, these immunohistochemical findings validate the pathway analysis
314 predictions and establish both conserved adaptive programs (NR4A3, EGFR, STAT1, PGC-
315 1α) and graft-type–specific regulatory signatures (IGF1/RUNX2 in arterial grafts;
316 RETN/SRC/PTGES in venous grafts) that operate during vascular graft adaptation to arterial
317 circulation.
318

319 **EGFR–STAT3 Signaling Differences Between VGP and VGO**

320 Upstream regulator analysis predicted preferential activation of EGFR in VGP, identifying
321 EGFR as a key regulatory node with predicted inhibitory effects on STAT3 (Figure 5A). This
322 prediction aligns with prior immunohistochemical findings (Figure 4C), which demonstrate

elevated EGFR expression in VGP and AGP, whereas VGO exhibits marked EGFR downregulation.

To evaluate the corresponding STAT3 response, immunohistochemical staining was performed (Figure 5B). VGP displayed minimal STAT3 nuclear positivity, whereas VGO demonstrated pronounced STAT3 upregulation within the fibrotic neointima. Quantitative analysis revealed a trend toward higher STAT3 expression in VGO (P=0.08), supporting reciprocal signaling dynamics characterized by EGFR-dominant/STAT3-suppressed activity in patent grafts versus STAT3-dominant activation in occluded grafts.

Angiotensin Activation and ECM Remodeling in VGO

Upstream regulator analysis comparing VGP and VGO identified angiotensinogen as one of the most strongly activated regulatory nodes associated with graft failure (Figure 5C). This activation was accompanied by the coordinated upregulation of multiple extracellular matrix–related proteins in VGO. The angiotensin-centered regulatory network (Figure 5D) revealed elevated expression of fibrillar collagens (COL5A1, COL5A2), small leucine-rich proteoglycans (decorin, biglycan, lumican), and thrombospondin-2, which collectively promote collagen fibrillogenesis and matrix stabilization. Regulator-effects modeling predicted enhanced matrix tensile strength as a downstream consequence in VGO, consistent with maladaptive fibrotic remodeling and reduced vascular compliance.

To validate these proteomic predictions, immunohistochemical staining for angiotensinogen was performed on matched VGP and VGO sections (Figure 5E). VGP exhibited minimal angiotensinogen immunoreactivity, showing only faint background staining. In contrast, VGO demonstrated marked angiotensinogen accumulation throughout the media and adventitia, with intense deposition in regions of dense extracellular matrix expansion and structural distortion. Quantitative analysis confirmed significantly elevated

348 angiotensinogen expression in VGO compared with VGP (P<0.01), supporting the
349 association between angiotensin pathway activation and fibroinflammatory remodeling in
350 failed grafts.
351
352 **Enhanced eNOS Expression in Luminal and Adventitial Neovascular Endothelial Cells**
353 **Following Arterial Grafting**
354 Expression of eNOS was evaluated by immunohistochemical staining across all vessel groups
355 (Figure 6A). AC and VC demonstrated weak to moderate eNOS immunoreactivity in the
356 luminal endothelium. Both AGP and VGP showed markedly elevated eNOS expression,
357 whereas VGO showed minimal signal, consistent with near-complete endothelial denudation.
358 Single-cell optical density analysis demonstrated enhanced eNOS expression in patent
359 grafts. Histogram distributions showed rightward shifts in AGP and VGP compared with
360 their respective controls (Figure 6B). Using a threshold of mean DAB optical density > 0.2,
361 the proportion of eNOS-positive cells was significantly higher in AGP versus AC (P<0.001)
362 and in VGP versus VC (P<0.01) (Figure 6C), distinguishing successfully adapted conduits
363 from failed grafts.
364
365 **Adventitial Neovascularization and Associated Upregulation of eNOS**
366 To evaluate adaptive remodeling of the vessel wall, we quantified CD31-positive adventitial
367 neovascularization (Figure S1E–H). Total microvascular content, measured as the cumulative
368 CD31-positive vessel perimeter, was significantly higher in AGP compared with AC
369 (P<0.001). Venous grafts showed a trend toward increased vasa vasorum relative to VC,
370 although this did not reach statistical significance. VGO demonstrated markedly reduced
371 adventitial microvascular density (Figure 6D).

372 Notably, robust eNOS immunoreactivity was observed in the endothelial cells lining
373 adventitial neovessels of patent grafts (Figure 6E, arrows). Quantification of eNOS-positive
374 microvessels—defined by endothelial DAB staining with nuclear co-localization—revealed
375 significant increases in AGP vs. AC and in VGP vs. VC (Figure 6F). VGO exhibited a
376 marked reduction in eNOS-positive neovessels, suggesting that eNOS expression in both
377 luminal and adventitial endothelium is associated with graft patency.
378

DISCUSSION

By leveraging a unique opportunity to analyze patent arterial and venous grafts explanted en bloc during cardiac transplantation, we provide the first comprehensive molecular characterization of successful graft adaptation in humans. Our findings challenge the traditional concept of venous "arterialization" and reveal that both arterial and venous grafts converge toward a shared adaptive phenotype characterized by coordinated activation of biosynthetic, vasoprotective, and stress-responsive pathways. We also identified specific molecular signatures—including NR4A3, STAT1, EGFR, and eNOS upregulation—that distinguish patent from occluded grafts, and demonstrate that angiotensinogen-driven fibroinflammatory remodeling is associated with graft failure. These findings provide a mechanistic framework for developing targeted therapies to enhance graft durability and improve long-term outcomes following CABG.

Histological Signatures of Graft Adaptation

While previous studies have predominantly focused on pathological processes leading to graft failure[16], our histological analysis of functionally patent grafts reveals adaptive remodeling signatures that have been largely overlooked in the literature. Traditional conceptualizations of vein graft adaptation have emphasized "arterialization" as a unidirectional transformation toward an arterial phenotype[3]. However, our findings demonstrate that both arterial and venous grafts undergo substantial structural reorganization that does not simply recapitulate native arterial architecture.

We found that arterial grafts, rather than preserving their native elastic artery characteristics, transitioned toward a muscular artery-like configuration characterized by marked medial thickening and an augmented internal elastic lamina. In contrast, venous grafts developed features absent in native veins—including a prominent internal elastic

lamina, extensive medial muscularization accompanied by elastic fiber deposition, and the formation of a novel external elastic layer. Most strikingly, despite their distinct embryological origins and baseline morphologies, both graft types converged toward similar caliber and structural organization while retaining unique architectural features not found in either native arteries or veins. This morphological convergence, coupled with the preservation of graft-specific characteristics, challenges the classical paradigm of simple arterialization and instead supports the emergence of a distinct adaptive phenotype uniquely tailored to the extraordinary hemodynamic demands of the coronary circulation. In this setting, grafts are subjected to intense pulsatile stress as the first major branches arising directly from the aortic root, receiving the full force of ventricular ejection without the dampening effect experienced by more distal vascular territories. In contrast, occluded grafts failed to achieve this adaptive remodeling, exhibiting severe aneurysmal dilatation, loss of elastic integrity, and medial necrosis — indicating that successful adaptation requires coordinated structural reorganization rather than passive exposure to arterial flow.

Adaptive Versus Pathologic Intimal Hyperplasia in Vein Grafts

Intimal hyperplasia has traditionally been regarded as a pathological hallmark of vein graft failure in CABG, contributing to progressive luminal narrowing and eventual occlusion[17]. However, our findings fundamentally challenge this binary perspective by demonstrating that substantial intimal thickening occurs in both functionally patent and occluded grafts, albeit with markedly distinct structural and cellular phenotypes. Patent grafts exhibited well-organized intimal architecture with preserved luminal patency, suggesting that intimal hyperplasia may represent an adaptive, actively regulated biological response essential for successful graft remodeling rather than an inherently pathological process.

This reconceptualization is strongly supported by previous studies. Jiang and colleagues, using a bilateral jugular vein graft model that exposed grafts to varying hemodynamic conditions, demonstrated that intimal hyperplasia develops as an adaptive response to mechanical stress; their findings showed that grafts maintain patency through coordinated outward remodeling[18]. Similarly, a recent animal study has reported that patent grafts exhibit concurrent intimal hyperplasia alongside positive remodeling—characterized by lumen preservation despite wall thickening—indicating that intimal hyperplasia is a component of successful environmental adaptation rather than an inevitable pathological process[19]. Histologically, patent grafts in our cohort exhibited a structurally organized intima with well-preserved endothelial integrity and a clearly demarcated internal elastic lamina, as demonstrated by elastic tissue staining. Notably, α-SMA-positive myofibroblasts were consistently identified within the intima of patent grafts, indicating controlled fibromuscular remodeling mediated by tightly regulated cellular proliferation and differentiation. The mechanistic role of myofibroblasts in adaptive intimal remodeling has been elegantly elucidated by Vasudevan and colleagues through ultrastructural analyses of rat vein grafts[20]. They documented that adventitial fibroblasts undergo coordinated migration into the intima and subsequent differentiation into myofibroblasts, which facilitate intimal thickening through organized matrix synthesis. Importantly, their ultrastructural findings revealed that adaptive intimal thickening comprises well-organized, multilayered myofibroblast assemblies rather than disorganized collagenous fibrosis—observations that closely align with our immunohistochemical characterization of human patent grafts. In contrast, occluded grafts exhibited profoundly disorganized intimal architecture, fragmented elastic laminae, and excessive extracellular matrix deposition without coordinated cellular organization. This distinction underscores that the qualitative characteristics of intimal hyperplasia—rather than merely its presence or extent—determine the long-term fate of the graft.

453 **Embryonic Arterialization Signaling**

454 The convergent adaptive remodeling observed in both arterial and venous grafts may reflect
455 the reactivation of embryonic arterialization signaling pathways. During vascular
456 development, arterial identity is established through the coordinated activation of VEGF-
457 Notch-ERK signaling cascades, which promote arterial-specific gene expression and
458 structural maturation. This developmental program is particularly well-characterized in
459 coronary artery embryogenesis, where VEGFR2-ERK-eNOS and NOTCH4 signaling axes
460 are distinctly upregulated and activated in endothelial cells during vascular morphogenesis[21–
461 23]. Specifically, VEGFR2 signaling activates the downstream ERK pathway, which is critical
462 for endothelial proliferation, branching morphogenesis, and lumen formation in both
463 coronary and general vascular embryology. eNOS is also upregulated and activated
464 downstream of VEGFR2 in response to VEGF stimulation in the endothelium, mediating
465 vasodilation and angiogenic responses required for vessel remodeling. Regarding NOTCH4,
466 this receptor (along with NOTCH1) is specifically expressed in embryonic vascular
467 endothelium and becomes markedly upregulated and activated during arterial specification
468 and network patterning. Activation of NOTCH4 in endothelial cells is essential for correct
469 branching morphogenesis and vascular patterning in the developing embryo, including the
470 coronary vasculature, with increased NOTCH4 expression further supporting arterial
471 specification from progenitor cells[22,23]

472 Our proteomic analysis revealed that patent grafts exhibited significant enrichment of
473 key components of the developmental arterialization program: VEGFR2 signaling (Figure 3A
474 and Figure S9B), ERK1/2 MAPK pathways (FDR$<5\times10^{-4}$; Supplementary Data), and
475 NOTCH4 signaling across all comparison groups, with consistently positive directionality
476 (AGP vs. AC: z-score=3.317; VGP vs. VC: z-score=2.673; VGP vs. VGO: z-score=4.472).
477 This pathway enrichment was accompanied by enhanced eNOS expression in both the

478 luminal endothelium and adventitial neovessels (Figure 6). The concurrent activation of
479 VEGFR2-ERK-eNOS and NOTCH4 pathways—mirroring the signaling architecture that
480 drives arterial specification during coronary embryogenesis—strongly supports the
481 hypothesis that successful graft adaptation involves partial recapitulation of developmental
482 arterialization programs. This coordinated pathway reactivation may represent an
483 evolutionarily conserved adaptive mechanism whereby adult vessels redeploy embryonic
484 programs to achieve structural and functional optimization under hemodynamic stress.
485
486
487 **Graft Failure is Characterized by Angiotensin-Driven Fibroinflammatory Remodeling**
488 **and Loss of Biosynthetic Resilience**
489 Our upstream regulator and regulator effects analysis identified angiotensin as a key activated
490 node in occluded vein grafts. The angiotensin-centered network predicted a coordinated
491 upregulation of extracellular matrix proteins (COL5A1, COL5A2, DCN, BGN, LUM,
492 THBS2), consistent with fibrotic remodeling and reduced vascular compliance.
493 Immunohistochemistry confirmed increased angiotensin expression in the medial and
494 adventitial regions of occluded vein grafts, supporting the hypothesis of an angiotensin-
495 driven fibroinflammatory remodeling mechanism underlying graft occlusion in our cohort.
496 This observation aligns with mechanistic insights from the renin-angiotensin system
497 literature: angiotensin II mediates vascular remodeling through vascular smooth muscle cell
498 proliferation, migration, extracellular matrix production, inflammation, and oxidative stress,
499 and is implicated in the pathogenesis of intimal hyperplasia and graft degeneration[24].
500 Moreover, polymorphism studies of the angiotensin-converting enzyme (ACE) gene in
501 saphenous vein graft atherosclerosis further support a link between angiotensin signaling and
502 graft pathology[25]. Given that we observed significantly greater luminal deposition of

503 angiotensin in occluded grafts compared to patent grafts, our data strengthen the hypothesis
504 that angiotensin signaling is not merely a bystander but may function as an upstream driver of
505 graft failure.

506 From a therapeutic perspective, although no large randomized trials have specifically
507 evaluated angiotensin blockade for improving saphenous vein graft patency, preclinical and
508 indirect clinical evidence suggest that targeting the renin-angiotensin axis may be beneficial.
509 For example, ACE inhibitors and angiotensin receptor blockers (ARBs) reduce vascular
510 remodeling and intimal hyperplasia in experimental models[24]. Observational analyses in post-
511 CABG populations have examined ACE inhibitor use, with one cohort study reporting that
512 post-CABG ACE/ARB therapy was associated with a lower hazard of major adverse
513 cardiovascular events at 1 and 5 years[26]. Although this does not directly measure graft-
514 specific patency, it is biologically plausible that the beneficial effect partly reflects improved
515 graft adaptation.

516 Thus, in light of our finding that angiotensin accumulation is specifically associated with
517 occluded grafts—and that this pattern corresponds to a predicted upstream regulatory
518 network driving extracellular matrix remodeling—we propose that angiotensin signaling
519 represents a novel, modifiable pathway in graft failure.

520

521 **Potential Role of eNOS in Perivascular Adipose Tissue as a Key Vasoprotective**
522 **Modulator**

523 eNOS is a key regulator of vascular homeostasis, mediating anti-thrombotic, anti-
524 inflammatory, and vasodilatory effects that maintain conduit integrity. Previous clinical and
525 experimental studies have demonstrated that increased eNOS activity within the luminal
526 endothelium correlates with improved graft patency and reduced vascular complications in
527 saphenous vein grafts used for coronary bypass surgery[27,28]. However, these investigations

528 have primarily focused on endothelial eNOS localized to the main vessel lumen, without
529 exploring its potential roles in the perivascular compartment.
530 In our study, we identified a distinct spatial pattern of eNOS upregulation extending
531 beyond the endothelium to the adventitia and PVAT in patent saphenous vein grafts. Notably,
532 intense eNOS expression was observed in the vasa vasorum and surrounding supportive
533 structures—an expression pattern absent in pre-implantation segments. This finding suggests
534 that the PVAT-adventitial domain may actively participate in graft adaptation, serving as a
535 secondary vasoprotective interface that complements luminal endothelial function.
536 PVAT is a metabolically active layer that release paracrine mediators—such as
537 adipokines and hydrogen sulfide—which enhance eNOS activity and exert anti-inflammatory
538 and anti-fibrotic effects on the vascular wall. Our histological evidence supports the concept
539 that preserving PVAT during no-touch vein harvesting not only maintains endothelial
540 integrity but also preserves an eNOS-enriched microenvironment within the perivascular
541 compartment. This dual-source nitric oxide signaling likely contributes to the superior long-
542 term patency observed with the no-touch technique.
543
544 **Limitations and Future Study**
545 This study has several limitations that warrant acknowledgment. First, the number of
546 available graft specimens was limited, reflecting the rarity and clinical challenges of
547 obtaining well-preserved human graft tissues explanted during cardiac transplantation.
548 Despite the small cohort size, each sample provided valuable biological insights into long-
549 term graft adaptation—a phenomenon rarely accessible in human studies. Second, surgical
550 techniques were not fully standardized across cases; variations in harvesting methods and
551 anastomotic configurations, including Y-graft constructs, may have influenced hemodynamic
552 and remodeling responses. Third, all molecular analyses were performed on bulk tissue,

553 precluding cell type- and layer-specific resolution. Although immunohistochemistry provided
554 partial spatial context for key markers such as eNOS, it could not fully delineate molecular
555 signals originating from distinct vascular compartments, including the intima, media, and
556 adventitia.

557 To address these limitations, future studies should incorporate spatially resolved
558 molecular profiling techniques—such as spatial transcriptomics and proteomics—to
559 characterize cell type- and layer-specific remodeling signatures within arterial and venous
560 grafts. Particular emphasis should be placed on the intimal compartment, where
561 hemodynamic and metabolic cues converge to influence the trajectory of intimal remodeling.
562 Spatial omics approaches will be essential for identifying the molecular regulators that
563 determine whether intimal proliferation stabilizes adaptively or progresses toward
564 pathological occlusion. Integrating these spatial insights with functional validation in
565 experimental graft models will enhance mechanistic understanding and guide the
566 development of targeted therapeutic strategies to improve long-term graft patency.
567

568 **Conclusion**

569 In this study, we found that arterial and venous grafts with long-term patency undergo a
570 convergent remodeling process and establish a distinct, graft-specific adaptive phenotype
571 characterized by structural maturation, reconstitution of elastic architecture, and a shared
572 biosynthetic-proteomic program uniquely shaped by the extraordinary hemodynamic
573 environment of the coronary circulation. Adventitial eNOS-positive neovascularization
574 emerged as a hallmark of adaptive remodeling, suggesting a vasoprotective mechanism that
575 sustains graft homeostasis. Collectively, these findings identify a biosynthetic-vasoprotective
576 remodeling axis as a central determinant of graft durability and propose that therapeutic

modulation of shared adaptive pathways may enhance long-term graft patency following coronary artery bypass grafting.

SOURCES OF FUNDING

This study was supported by grant No 0420254100 [2025–3000] from the SNUH Research Fund; and a focused clinical research grant-in-aid from the Seoul Metropolitan Government Seoul National University (SMG-SNU) Boramae Medical Center (04-2023-0005).

DISCLOSURES

None.

SUPPLEMENTAL MATERIAL

SUPPLEMENTAL METHODS

SUPPLEMENTAL RESULTS

Tables S1 and S2

Figures S1–S14

REFERENCES

1. Gharibeh L, Ferrari G, Ouimet M, Grau JB. Conduits' Biology Regulates the Outcomes of Coronary Artery Bypass Grafting. *JACC: Basic Transl Sci*. 2021;6(4):388-396. doi:10.1016/j.jacbts.2020.11.015

2. Taggart DP. Current status of arterial grafts for coronary artery bypass grafting. *Ann Cardiothorac Surg*. 2013;2(4):427-430. doi:10.3978/j.issn.2225-319x.2013.07.21

3. Muto A, Model L, Ziegler K, Eghbalieh SDD, Dardik A. Mechanisms of Vein Graft Adaptation to the Arterial Circulation. *Circ J*. 2010;74(8):1501. doi:10.1253/circj.cj-10-0495

4. Gaudino M, Benedetto U, Fremes S, Ballman K, Biondi-Zoccai G, Sedrakyan A, Nasso G, Raman J, Buxton B, Hayward PA, Moat N, Collins P, Webb C, Peric M, Petrovic I, Yoo KJ, Hameed I, Franco AD, Moscarelli M, Speziale G, Puskas JD, Girardi LN, Hare DL, Taggart DP, Investigators R. Association of Radial Artery Graft vs Saphenous Vein Graft With Long-term Cardiovascular Outcomes Among Patients Undergoing Coronary Artery Bypass Grafting. *JAMA*. 2020;324(2):179-187. doi:10.1001/jama.2020.8228

5. Cuminetti G, Gelsomino S, Curello S, Lorusso R, Maessen JG, Hoorntje JCA. Contemporary use of arterial and venous conduits in coronary artery bypass grafting: anatomical, functional and clinical aspects. *Neth Hear J*. 2017;25(1):4-13. doi:10.1007/s12471-016-0919-2

6. Gaudino M, Antoniades C, Benedetto U, Deb S, Franco AD, Giammarco GD, Fremes S, Glineur D, Grau J, He GW, Marinelli D, Ohmes LB, Patrono C, Puskas J, Tranbaugh R, Girardi LN, Taggart DP, Ruel M, Bakaeen FG. Mechanisms, Consequences, and Prevention

616 of Coronary Graft Failure. *Circulation*. 2017;136(18):1749-1764.
617 doi:10.1161/circulationaha.117.027597

618 7. Vries MR de, Simons KH, Jukema JW, Braun J, Quax PHA. Vein graft failure: from
619 pathophysiology to clinical outcomes. *Nat Rev Cardiol*. 2016;13(8):451-470.
620 doi:10.1038/nrcardio.2016.76

621 8. Dashwood MR, Savage K, Dooley A, Shi-Wen X, Abraham DJ, Souza DSR. Effect of
622 Vein Graft Harvesting on Endothelial Nitric Oxide Synthase and Nitric Oxide Production.
623 *Ann Thorac Surg*. 2005;80(3):939-944. doi:10.1016/j.athoracsur.2005.03.042

624 9. Bikdeli B, Hassantash SA, Pourabdollah M, Kalantarian S, Sadeghian M, Afshar H, Sabeti
625 S, Marzban M, Ahmadi H, Mohammadi F. Histopathologic Insight into Saphenous Vein
626 Bypass Graft Disease. *Cardiology*. 2012;123(4):208-215. doi:10.1159/000343269

627 10. Tian M, Wang X, Feng W, Wang H, Liu S, Liu Z, Chen Y, Miao Q, Su P, Li X, Wang Y,
628 Lu B, Chen K, Zhang C, Hu S. No-touch versus conventional vein in coronary artery bypass
629 grafting: three year follow-up of multicentre randomised PATENCY trial. *BMJ*.
630 2025;389:e082883. doi:10.1136/bmj-2024-082883

631 11. Mikami T, Dashwood MR, Kawaharada N, Furuhashi M. An Obligatory Role of
632 Perivascular Adipose Tissue in Improved Saphenous Vein Graft Patency in Coronary Artery
633 Bypass Grafting. *Circ J*. 2024;88(6):845-852. doi:10.1253/circj.cj-23-0581

634 12. Saito T, Kurazumi H, Suzuki R, Matsunaga K, Tsubone S, Lv B, Kobayashi S, Nagase T,
635 Mizoguchi T, Samura M, Suehiro K, Harada T, Morikage N, Mikamo A, Hamano K.
636 Perivascular Adipose Tissue Is a Major Source of Nitric Oxide in Saphenous Vein Grafts

637 Harvested via the No-Touch Technique. *J Am Hear Assoc: Cardiovasc Cerebrovasc Dis*.
638 2020;11(3):e020637. doi:10.1161/jaha.120.020637

639 13. Dashwood MR, Dooley A, Shi-Wen X, Abraham DJ, Souza DSR. Does Periadventitial
640 Fat-Derived Nitric Oxide Play a Role in Improved Saphenous Vein Graft Patency in Patients
641 Undergoing Coronary Artery Bypass Surgery? *J Vasc Res*. 2007;44(3):175-181.
642 doi:10.1159/000099833

643 14. Szklarczyk D, Gable AL, Nastou KC, Lyon D, Kirsch R, Pyysalo S, Doncheva NT,
644 Legeay M, Fang T, Bork P, Jensen LJ, Mering C von. The STRING database in 2021:
645 customizable protein–protein networks, and functional characterization of user-uploaded
646 gene/measurement sets. *Nucleic Acids Res*. 2021;49(D1):D605-D612.
647 doi:10.1093/nar/gkaa1074

648 15. Zhou Y, Zhou B, Pache L, Chang M, Khodabakhshi AH, Tanaseichuk O, Benner C,
649 Chanda SK. Metascape provides a biologist-oriented resource for the analysis of systems-
650 level datasets. *Nat Commun*. 2019;10(1):1523. doi:10.1038/s41467-019-09234-6

651 16. Owens CD, Gasper WJ, Rahman AS, Conte MS. Vein graft failure. *J Vasc Surg*.
652 2015;61(1):203-216. doi:10.1016/j.jvs.2013.08.019

653 17. Goldstein DJ, Chang HL, Mack MJ, Voisine P, Gammie JS, Marks ME, Iribarne A,
654 Vengrenyuk Y, Raymond S, Taylor BS, Dagenais F, Ailawadi G, Chu MWA, DiMaio JM,
655 Narula J, Moquete EG, O'Sullivan K, Williams JB, Crestanello JA, Scavo V, Puskas JD,
656 Acker MA, Gillinov M, Gelijns AC, O'Gara PT, Moskowitz AJ, Alexander JH, Bagiella E.
657 Intimal hyperplasia, saphenous vein graft disease, and clinical outcomes: Insights from the
658 CTSN VEST randomized trial. *J Thorac Cardiovasc Surg*. 2024;167(5):1782-1792.e5.
659 doi:10.1016/j.jtcvs.2022.10.034

660 18. Jiang Z, Wu L, Miller BL, Goldman DR, Fernandez CM, Abouhamze ZS, Ozaki CK,
661 Berceli SA. A novel vein graft model: adaptation to differential flow environments. *Am J*
662 *Physiol-Hear Circ Physiol*. 2004;286(1):H240-H245. doi:10.1152/ajpheart.00760.2003

663 19. Yao G, Li H, Zuo X, Wang C, Xiao Y, Zhao Y, Wang X. Oscillatory shear stress
664 promotes vein graft intimal hyperplasia via NADPH oxidase-related pathways. *Front Surg*.
665 2023;10:1073557. doi:10.3389/fsurg.2023.1073557

666 20. Stark VK, Warner TF, Hoch JR. An ultrastructural study of progressive intimal
667 hyperplasia in rat vein grafts. *J Vasc Surg*. 1997;26(1):94-103. doi:10.1016/s0741-
668 5214(97)70152-6

669 21. Kroll J, Waltenberger J. VEGF-A Induces Expression of eNOS and iNOS in Endothelial
670 Cells via VEGF Receptor-2 (KDR). *Biochem Biophys Res Commun*. 1998;252(3):743-746.
671 doi:10.1006/bbrc.1998.9719

672 22. Luo W, Garcia-Gonzalez I, Fernández-Chacón M, Casquero-Garcia V, Sanchez-Muñoz
673 MS, Mühleder S, Garcia-Ortega L, Andrade J, Potente M, Benedito R. Arterialization
674 requires the timely suppression of cell growth. *Nature*. 2021;589(7842):437-441.
675 doi:10.1038/s41586-020-3018-x

676 23. Wythe JD, Dang LTH, Devine WP, Boudreau E, Artap ST, He D, Schachterle W, Stainier
677 DYR, Oettgen P, Black BL, Bruneau BG, Fish JE. ETS Factors Regulate Vegf-Dependent
678 Arterial Specification. *Dev Cell*. 2013;26(1):45-58. doi:10.1016/j.devcel.2013.06.007

679 24. Osgood MJ, Harrison DG, Sexton KW, Hocking KM, Voskresensky IV, Komalavilas P,
680 Cheung-Flynn J, Guzman RJ, Brophy CM. Role of the Renin–Angiotensin System in the

Pathogenesis of Intimal Hyperplasia: Therapeutic Potential for Prevention of Vein Graft Failure? *Ann Vasc Surg*. 2012;26(8):1130-1144. doi:10.1016/j.avsg.2011.12.001

25. Zeinali N, Hashemi M, Mirmohammadsadeghi M, Mirmohammadsadeghi H, Eskandari N, Sabzghabaee AM. Association of Angiotensin-Converting Enzyme Genotype, Insertion/Deletion Polymorphism and Saphenous Vein Graft Atherosclerosis in Iranian Patients. *Rev Bras Cir Cardiovasc*. 2015;30(5):557-561. doi:10.5935/1678-9741.20150069

26. Kalavrouziotis D, Buth KJ, Cox JL, Baskett RJ. Should all patients be treated with an angiotensin-converting enzyme inhibitor after coronary artery bypass graft surgery? The impact of angiotensin-converting enzyme inhibitors, statins, and β-blockers after coronary artery bypass graft surgery. *Am Hear J*. 2011;162(5):836-843. doi:10.1016/j.ahj.2011.07.004

27. Otsuka F, Yahagi K, Sakakura K, Virmani R. Why is the mammary artery so special and what protects it from atherosclerosis? *Ann Cardiothorac Surg*. 2013;2(4):519-526. doi:10.3978/j.issn.2225-319x.2013.07.06

28. Collins MJ, Li X, Lv W, Yang C, Protack CD, Muto A, Jadlowiec CC, Shu C, Dardik A. Therapeutic strategies to combat neointimal hyperplasia in vascular grafts. *Expert Rev Cardiovasc Ther*. 2012;10(5):635-647. doi:10.1586/erc.12.33

Figure Legends

Figure 1.

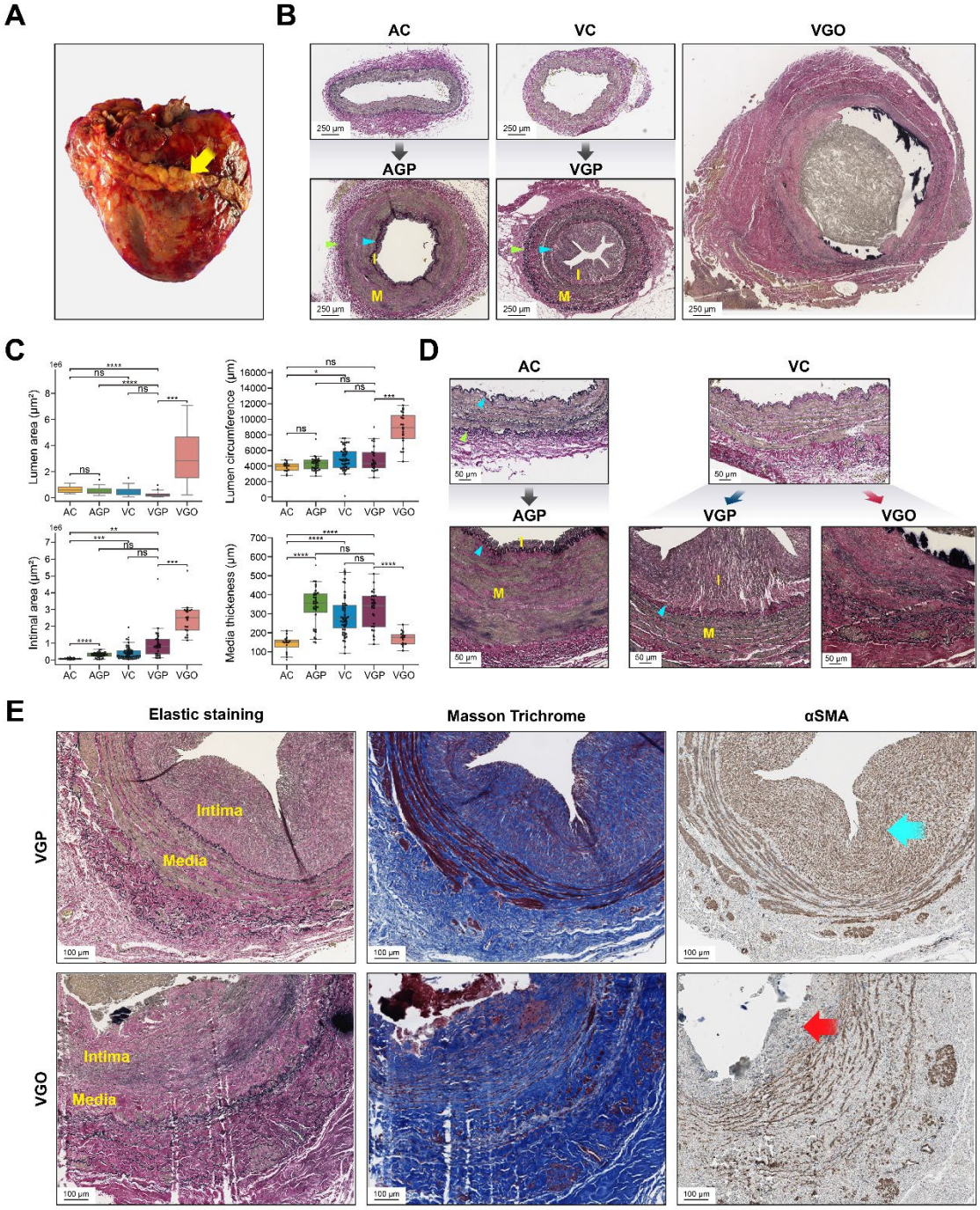

(A) Explanted heart with attached saphenous vein grafts harvested using the no-touch technique. Gross photograph of an explanted heart from a patient with prior coronary artery bypass grafting (yellow arrow). The saphenous vein graft conduits remain attached to the

705 heart, with perivascular supportive tissue preserved as a result of the no-touch harvesting
706 technique.
707 (B) Histomorphologic remodeling of arterial and venous conduits following grafting.
708 Blue arrowheads indicate the internal elastic lamina, marking the boundary between the
709 intima (I) and media (M). Green arrowheads indicate the external elastic lamina, marking the
710 boundary between the media (M) and adventitia. Yellow labels denote the intima (I) and
711 media (M) within each graft.
712 (C) Quantitative morphometric analysis of arterial and venous graft remodeling.
713 Boxplots show the lumen area (upper left), lumen circumference (upper right), intimal area
714 (lower left), and medial thickness (lower right) across native arterial conduits (AC), arterial
715 grafts (AGP), native venous conduits (VC), patent venous grafts (VGP), and occluded venous
716 grafts (VGO). Statistical comparisons are indicated above each plot (*P<0.05; **P<0.01;
717 ***P<0.001; ****P<0.0001; ns, not significant).
718 (D) Intimal and medial morphology across arterial and venous graft states.
719 Elastic staining of native arteries (AC) and veins (VC), their patent graft counterparts (AGP,
720 VGP), and occluded vein grafts (VGO).
721 (E) Histochemical and immunohistochemical characteristics of patent versus occluded vein
722 grafts.
723 Elastic staining showed a well-organized intima–media structure in patent vein grafts (VGP),
724 whereas occluded grafts (VGO) exhibited disrupted elastic layers. Masson Trichrome
725 staining demonstrated structured fibrosis with preserved layering in VGP, but dense,
726 disorganized collagen in VGO. αSMA staining revealed abundant, organized smooth muscle–
727 type cells in the VGP intima (blue arrow) and near-complete absence of αSMA-positive cells
728 in the fibrotic VGO intima (red arrow).
729

730 **Figure 2**

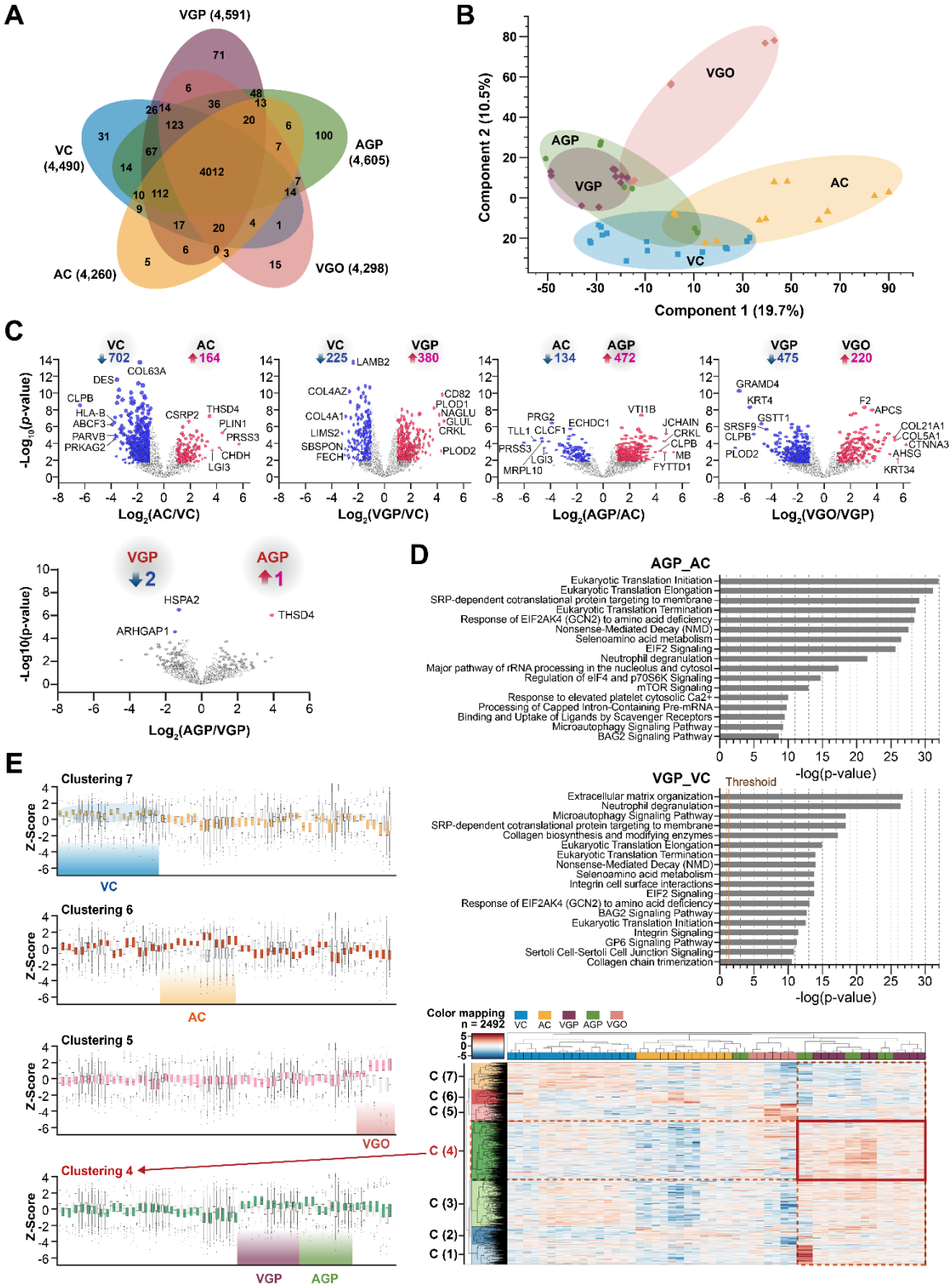

731

732 (A) Number of identified proteins

Venn diagram showing overlap of identified proteins across five vascular tissue groups. A total of 4,836 proteins were identified across all samples using mass spectrometry–based proteomic analysis. The five groups included vein control (VC, n=4,490 proteins), artery control (AC, n=4,260), patent vein grafts (VGP, n=4,591), patent artery grafts (AGP, n=4,605), and occluded vein grafts (VGO, n=4,298). Among these, 4,012 proteins were commonly detected across all five groups, while subsets of proteins were uniquely identified in specific conditions. The number of shared and group-specific proteins is indicated within each section of the Venn diagram.

(B) Unsupervised 2-dimensional PCA showing distinct clustering patterns across vascular groups. AC and VC samples separated widely along PC1, reflecting their differing baseline proteomic profiles. AGP and VGP samples clustered closely, indicating similar post-grafting proteomic changes. VGO samples formed a cluster that was distinct from both native vessels and patent grafts.

(C) Differential protein expression among native vessels and graft types.

Volcano plot comparing VC and AC showing 702 proteins enriched in VC and 164 enriched in AC, indicating clear baseline proteomic differences between veins and arteries. Comparison of AC and AGP identified 134 proteins enriched in AC and 472 enriched in AGP, consistent with extensive arterial graft remodeling. Comparison of VC and VGP revealed 225 proteins enriched in VC and 380 enriched in VGP, reflecting substantial remodeling following venous grafting. Direct comparison of AGP and VGP showed only a minimal number of differentially expressed proteins, underscoring the post-grafting similarity between arterial and venous conduits. Comparison of VGP and VGO identified 475 proteins enriched in VGP and 220 enriched in VGO, highlighting the molecular divergence between functional and occluded vein grafts.

(D) Canonical pathway enrichment analysis of arterial and venous grafts.

758 (Left) Canonical pathway enrichment analysis for AGP versus AC showed significant
759 activation of translation-related pathways (e.g., initiation, elongation, termination, and SRP-
760 dependent targeting), EIF2/GCN2 signaling, nonsense-mediated decay, and proteostasis-
761 associated programs, including microautophagy and BAG2 signaling.
762 (Right) Canonical pathway enrichment analysis for VGP versus VC showed similar
763 enrichment in translation-associated pathways, including EIF2/GCN2, and proteostasis
764 pathways, along with additional processes related to extracellular matrix organization,
765 collagen biosynthesis, integrin signaling, and neutrophil degranulation.
766 (E) Hierarchical clustering reveals group-specific proteomic signatures across vascular
767 samples. Clustering of the 2,492 most variable proteins generated distinct groups
768 corresponding to major vascular phenotypes. Cluster 7 consisted predominantly of VC
769 samples, while Cluster 6 was largely composed of AC samples, reflecting baseline proteomic
770 differences between native veins and arteries. Cluster 5 was enriched with VGO samples and
771 displayed a molecular pattern distinct from all other groups. Cluster 4 contained proteins
772 consistently upregulated in both AGP and VGP, highlighting the close similarity of
773 proteomic profiles in functional arterial and venous grafts.
774
775

Figure 3. Integrated functional analysis differentiates adaptive remodeling in patent grafts from maladaptive processes in occluded grafts.

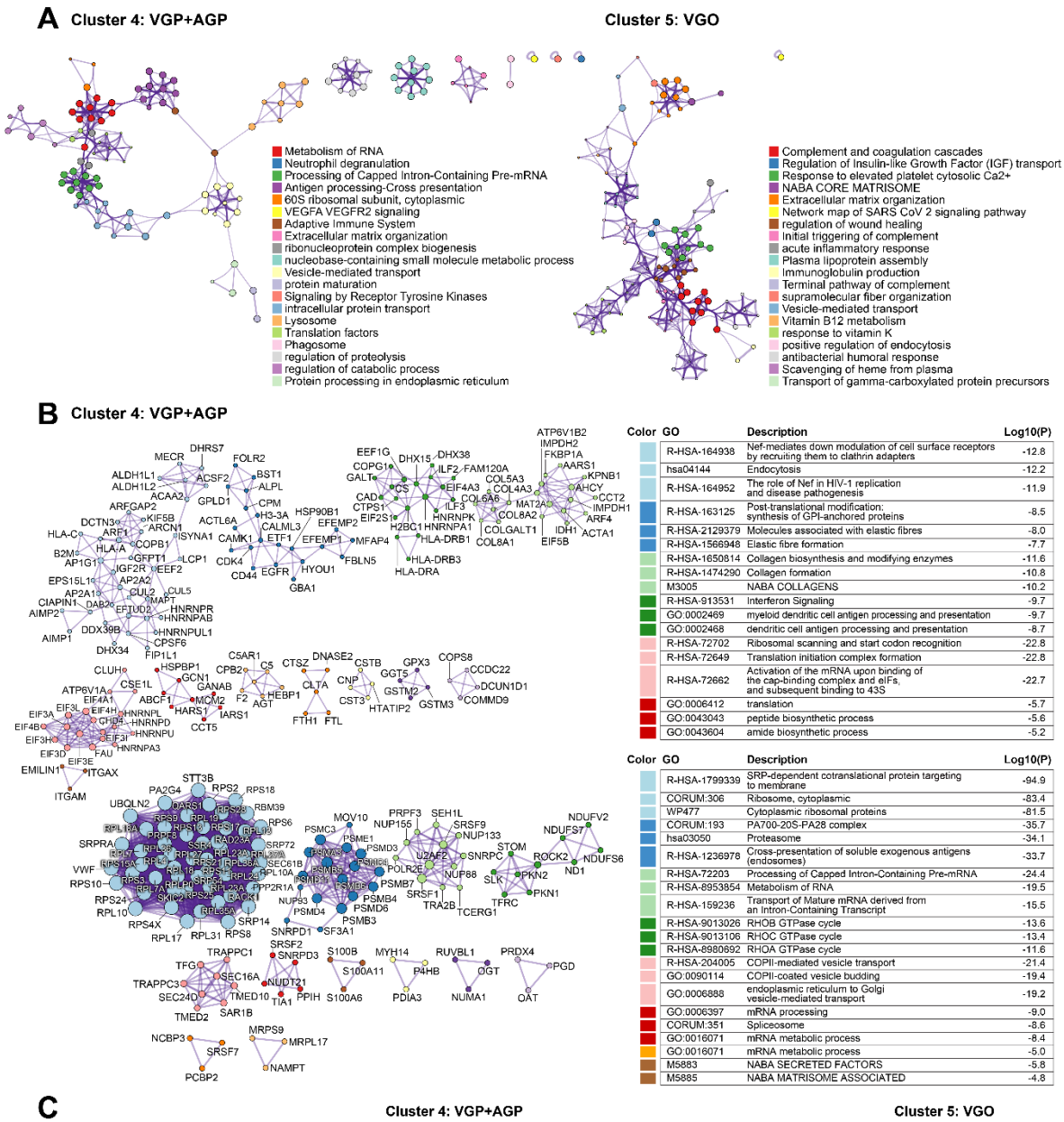

(A) Pathway enrichment analysis of Cluster 4 (VGP + AGP) and Cluster 5 (VGO).

Cluster 4 showed coordinated enrichment in RNA metabolism, mRNA processing, translation initiation/elongation, ribonucleoprotein biogenesis, and pathways supporting extracellular matrix (ECM) organization and cytoskeletal adaptation. In contrast, Cluster 5 exhibited predominant enrichment of complement and coagulation cascades, acute inflammatory signaling, wound healing, and disorganized ECM remodeling.

(B) Protein–protein interaction (PPI) networks for Cluster 4

Cluster 4 networks revealed densely interconnected ribosomal/translation hubs and organized ECM-remodeling subnetworks, consistent with an active, reparative remodeling phenotype.

(C) Metascape pathway enrichment analysis of functional and obstructed grafts (Cluster 4 and Cluster 5). Pathway enrichment analysis was conducted using Metascape (www.metascape.org), which integrates multiple curated ontologies, including GO, KEGG, and Reactome. (A) Pathways enriched in functional grafts, including vein graft patent (VGP) and artery graft patent (AGP) groups. (B) Pathways enriched in the vein graft obstructed (VGO) group. Each bubble represents a biological pathway, where the x-axis shows enrichment significance ($-\log_{10}$(q-value)), the y-axis shows pathway names, bubble size reflects the percentage of overlapping genes (Overlap%), and bubble color reflects significance strength, where a more intense pink indicates higher significance. Cluster 4 (VGP + AGP) demonstrated enrichment of pathways related to RNA metabolism, VEGFA–VEGFR2 signaling, receptor tyrosine kinase activity, protein maturation, intracellular transport, lysosomal processes, and immune-regulatory programs—reflecting a biosynthetically active, structurally adaptive, and immune-balanced phenotype characteristic of functional grafts. In contrast, Cluster 5 (VGO) was enriched for complement and coagulation pathways, NABA matrisome and ECM-associated programs, platelet activation, plasma lipoprotein assembly, and IGFBP-mediated IGF transport regulation—defining a

matrix-disruptive, thrombosis-prone, and growth factor–dysregulated environment associated with graft obstruction.

808 **Figure 4.** Upstream regulatory programs and immunohistochemical validation in arterial and

809 venous grafts

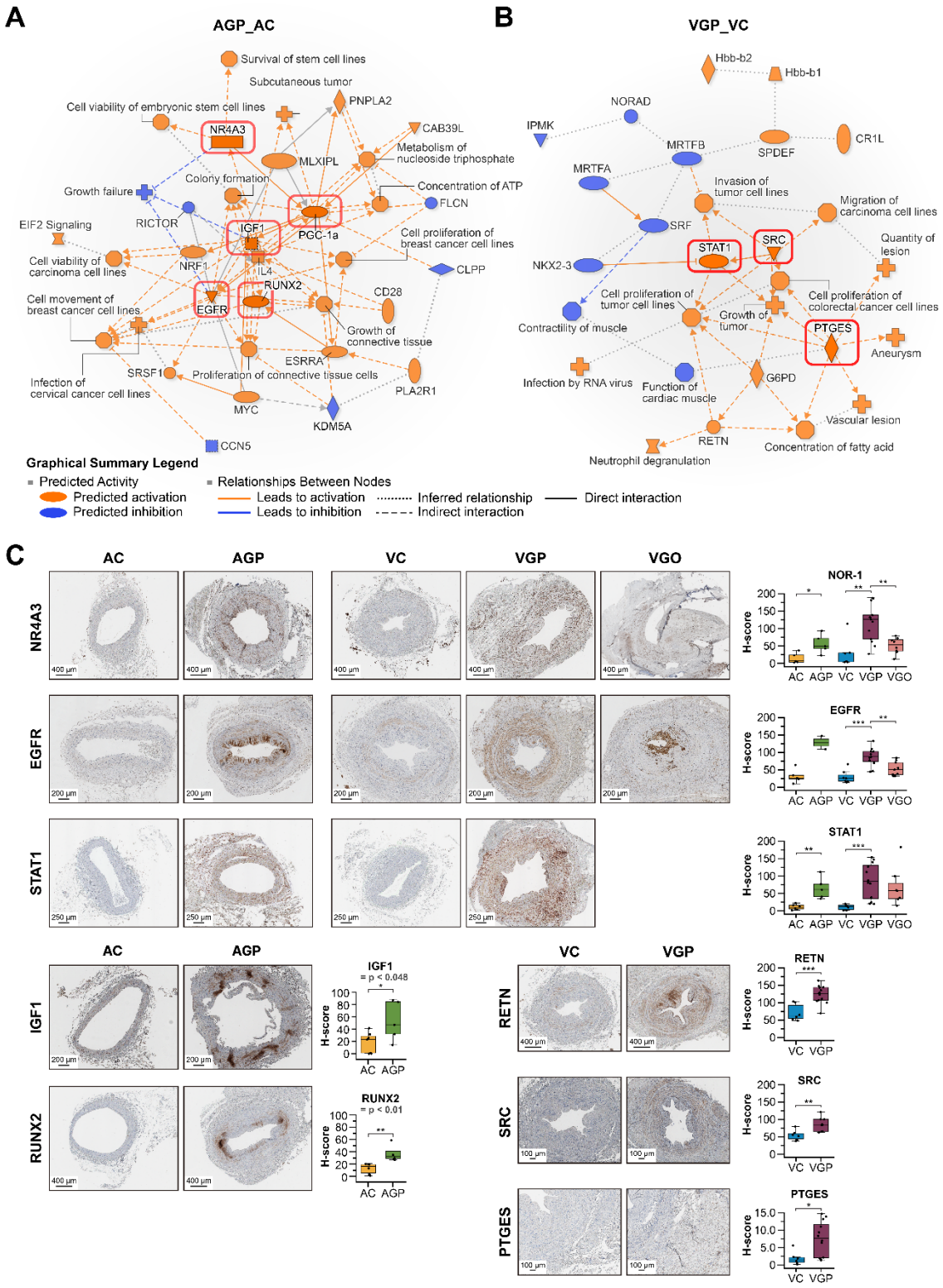

810

811 (A) Arterial grafts (AGP vs. AC). Upstream regulator analysis revealed coordinated

activation of metabolic and proliferative regulators, including IGF1, RUNX2, NR4A3, PGC-1α, EGFR, and MYC.

(B) Venous grafts (VGP vs. VC). Patent vein grafts showed activation of proliferative–biosynthetic regulators, including STAT1, SRC, PTGES, RETN, and G6PD, accompanied by predicted inhibition of vascular contractility regulators such as SRF and MRTFA—indicating a shift toward a synthetic, remodeling-competent phenotype.

(C) Immunohistochemical validation. IHC confirmed increased expression of NR4A3, EGFR, and STAT1 in both AGP and VGP ($p<0.01$), identifying these as conserved adaptive regulators across graft types. Arterial grafts showed specific upregulation of IGF1 and RUNX2, while venous grafts exhibited higher expression of RETN, SRC, and PTGES compared with their respective controls, validating graft-type–specific adaptive signaling predicted by upstream analyses.

826 **Figure 5.** Distinct upstream signaling patterns and angiotensin-associated extracellular matrix

827 remodeling in patent and occluded venous grafts

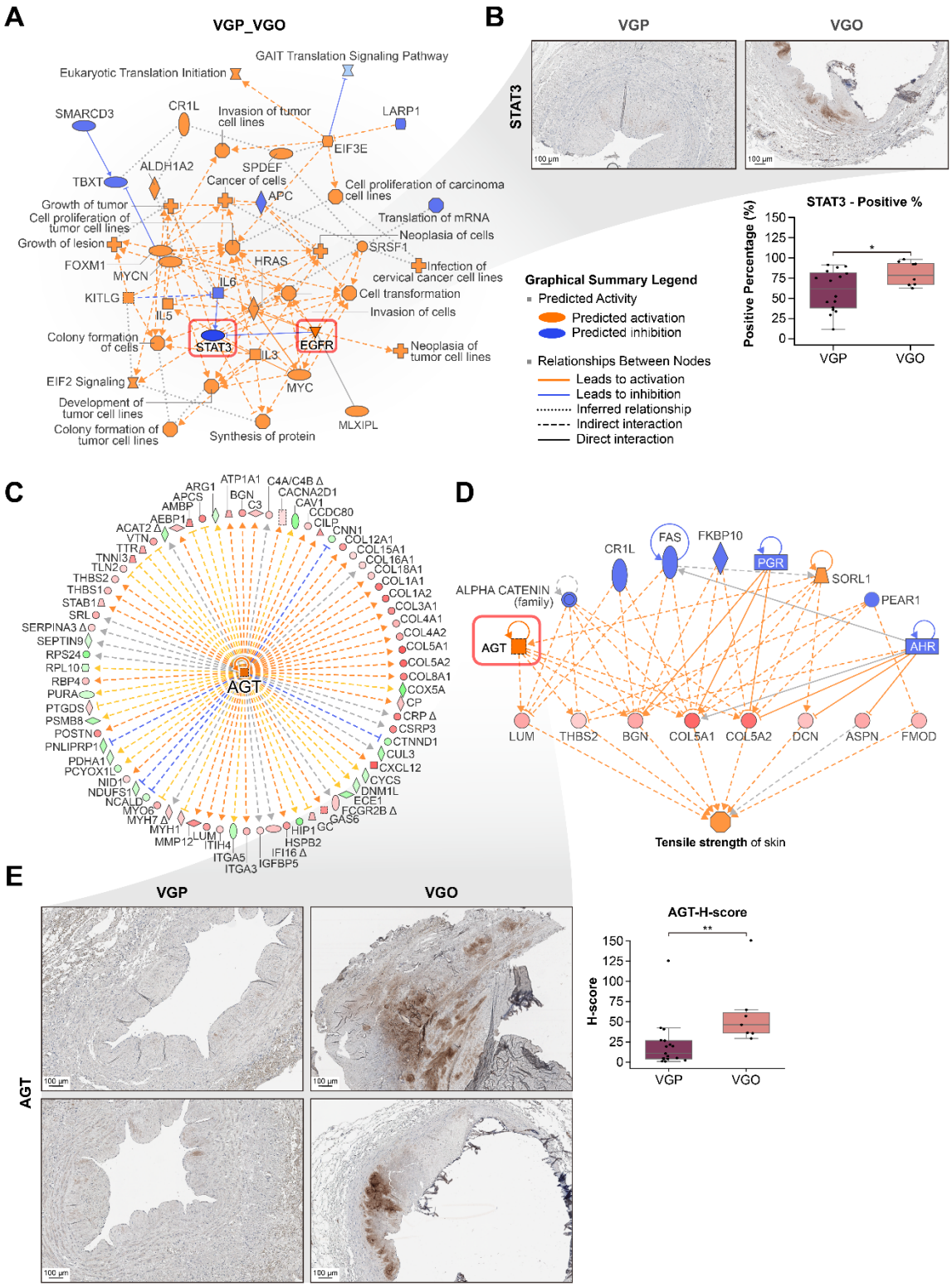

828

829 (A) Upstream regulator analysis comparing VGP and VGO using Ingenuity Pathway

830 Analysis. Orange nodes indicate predicted activated regulators, while blue nodes indicate
831 inhibited regulators. In VGP relative to VGO, STAT3 downregulation, coupled with
832 reciprocal EGFR upregulation, emerged as a key regulatory axis distinguishing successful
833 graft adaptation.
834 (B) STAT3 expression assessed by immunohistochemistry and quantitative analysis. Upper
835 panels: Representative STAT3 staining in VGP (left) and VGO (right) demonstrating
836 minimal STAT3 expression in patent grafts versus increased nuclear positivity in occluded
837 grafts. Scale bars=100 μm. Lower panel: Quantification of STAT3-positive cells showing a
838 trend toward elevated expression in VGO (P=0.08). n=8–10 per group.
839 (C) Upstream regulator analysis identified angiotensin as a central activated node in VGO.
840 The angiotensin-centered regulatory network illustrates predicted downstream targets related
841 to the extracellular matrix. Node size reflects network connectivity, while connecting edges
842 represent predicted regulatory or protein–protein interactions.
843 (D) Expanded angiotensin regulatory network highlighting extracellular matrix structural
844 proteins (orange), matrix-associated signaling molecules (blue), and downstream predicted
845 biological functions (pink). Color intensity reflects the predicted activation state. Upregulated
846 matrix components include fibrillar collagens (COL5A1, COL5A2), small leucine-rich
847 proteoglycans (decorin, biglycan, lumican), and thrombospondin-2, which collectively
848 contribute to enhanced matrix tensile strength in occluded grafts.
849 (E) Immunohistochemical validation of the expression of angiotensinogen, the precursor of
850 angiotensin. Left column: Two representative cases of patent venous grafts (VGP), each from
851 a different patient, demonstrating minimal angiotensinogen staining throughout the vessel
852 wall. Right column: Two representative cases of occluded venous grafts (VGO), each from a
853 different patient, showing prominent angiotensinogen deposition in the media and adventitia,
854 with dense accumulation within fibrotic regions. All images are at the same magnification.

855 Scale bars=200 μm. Right panel: Quantitative H-score analysis revealed significantly
856 elevated angiotensinogen expression in VGO versus VGP (**P<0.01). Box plots display the
857 median and interquartile range (n=8–12 per group).
858
859

Figure 6. Upregulation of eNOS in luminal and adventitial endothelial cells in arterial grafts

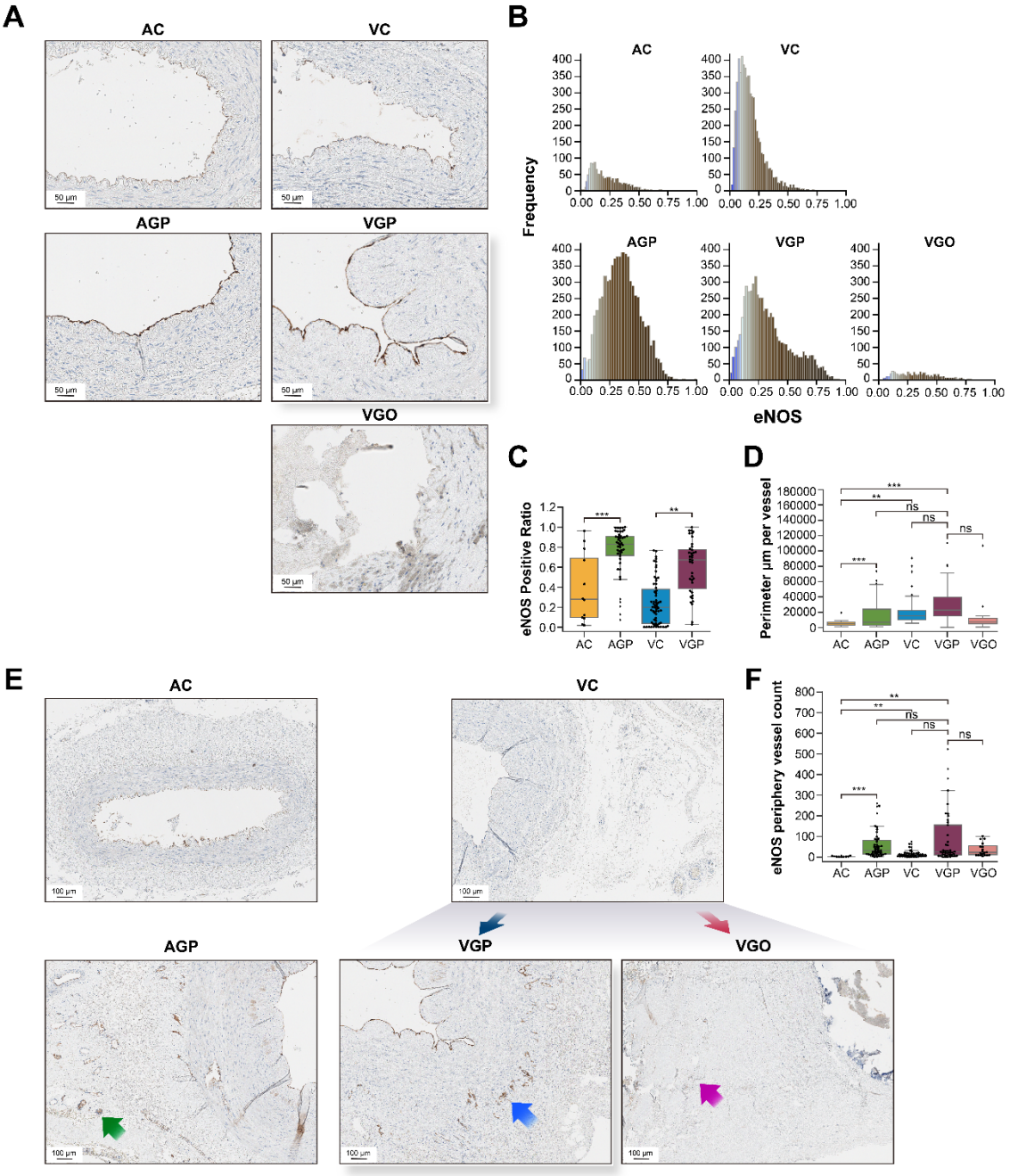

(A-C) eNOS expression in the luminal endothelium.

(A) Representative immunohistochemistry showing weak eNOS expression in control vessels (AC, VC) and marked upregulation in patent grafts (AGP, VGP). Occluded grafts (VGO) exhibit endothelial denudation with minimal eNOS signal. Scale bars=50 µm.

(B) Histogram analysis of single-cell optical density revealed a rightward shift in the graft endothelium, indicating enhanced eNOS expression.

(C) Proportion of eNOS-positive cells (optical density >0.2) was significantly higher in AGP versus AC (***P<0.001) and in VGP versus VC (**P<0.01).

(D, E) eNOS expression in the adventitial vasa vasorum.

(D) Representative images show enhanced neovascularization with eNOS-positive endothelium in AGP (green arrow) and VGP (cyan arrow) compared with controls. VGO (magenta arrow) demonstrated sparse vasculature lacking eNOS expression. Scale bars=100 μm.

(E) Left: Total microvascular perimeter was significantly larger in AGP versus AC (***P<0.001). Right: eNOS-positive adventitial vessel count was significantly higher in AGP versus AC (***P<0.001) and in VGP versus VC (**P<0.01). Box plots display median and interquartile range. Statistical analysis was performed using one-way ANOVA with Tukey's post hoc test.

ONLINE SUPPLEMENT

SUPPLEMENTAL METHODS

Proteomic Analysis of FFPE Graft Tissues

Sample Preparation and Protein Extraction

For proteomic profiling, FFPE tissue sections (5 µm thick, five serial sections per sample) were prepared from 5 VGP, 3 VGO, 4 AGP, 8 VC, and 6 AC blocks and collected into LoBind tubes (Sigma-Aldrich). Samples were deparaffinized and lysed in a buffer containing 5% sodium dodecyl sulfate and 50 mM triethylammonium bicarbonate (TEAB, pH 8.5), then incubated at 50°C for 20 minutes. Sample disruption and protein extraction were performed using the Covaris R220 Focused-Ultrasonicator (Covaris, Woburn, MA). Adaptive Focused Acoustics conditions were set to 175 W, 10% duty factor, 200 cycles/burst at 20 °C for 300 seconds, followed by incubation at 80 °C for 1 h.

Reduction (20 mM dithiothreitol, 56°C for 10 minutes) and alkylation (40 mM iodoacetamide, 30 minutes in the dark at room temperature) were performed, followed by a second acoustic treatment (360 seconds). Protein concentrations were measured via Bradford assay (Thermo Fisher). Protein digestion was carried out using the Suspension Trap (S-Trap, Profiti) protocol. After acidification with phosphoric acid and binding in methanol/TEAB buffer, proteins were trapped, washed, and sequentially eluted with TEAB, 0.2% formic acid, and 0.2% formic acid/50% acetonitrile. The eluates were vacuum-dried and stored at –80°C.

LC-MS/MS Acquisition and Protein Identification

Peptides were analyzed using a Vanquish Neo LC system coupled with an Orbitrap Eclipse mass spectrometer (Thermo Fisher Scientific). Samples (4 µL, 0.5 µg/µL) were injected into a

PepMap C18 trap column and separated on a PepMap Neo analytical column (75 µm × 500 mm, 2 µm, 100 Å) at a flow rate of 300 nL/min over 180 minutes. A gradient of 3–25% solvent B over 150 minutes, 25–80% B over 10 minutes, and 80% B for 20 minutes was applied (mobile phases: 0.1% formic acid in water or acetonitrile). The Orbitrap operated in data-dependent acquisition mode with MS1 resolution set to 120,000, scan range of 375–1800 m/z, and FAIMS compensation voltages of –45, –55, and –75 V. MS2 spectra were acquired in the ion trap using turbo scan mode (AGC target 300%, maximum injection time 15 ms, normalized collision energy 35%).

Database Search and Quantification

Raw files were analyzed using SEQUEST-HT in Proteome Discoverer v2.4 against the UniProt-SwissProt human database. Search parameters included a 10 ppm precursor tolerance and a 0.6 Da fragment tolerance, allowing for two missed cleavages. Carbamidomethylation was set as a fixed modification, and methionine oxidation as a variable modification. The false discovery rate (FDR) was estimated using a target-decoy strategy and controlled at <1% using Percolator.

Label-free quantification (LFQ) was performed based on precursor ion intensities of unique and razor peptides, excluding oxidized methionine. LFQ values were $\log_2$-transformed, normalized using width adjustment, and imputed with a normal distribution model. Proteins detected in all replicates of at least one group were retained. Principal component analysis (PCA) was conducted using Perseus (v1.6.2.3).

Data visualization and exploratory clustering analyses were performed with Instant Clue, including volcano plots, correlation plots, hierarchical heatmaps, and cluster box plots. Hierarchical clustering was carried out using Distance=Correlation and Linkage=Complete.

Sparse partial least squares–discriminant analysis (sPLS-DA) was performed using MetaboAnalyst (www.metaboanalyst.ca). Upset plots were generated with the ComplexUpset R package (v1.3.3) implemented in RStudio (2024.12). Pathway enrichment analyses were conducted using Metascape (https://metascape.org) and Ingenuity Pathway Analysis (IPA, QIAGEN Inc.).

Canonical Pathway Analysis

Canonical pathway enrichment was conducted using the Core Analysis function in IPA (QIAGEN) on differentially expressed proteins (DEPs) between graft groups. The directional interpretation of pathway activity was based on the IPA z-score metric, which integrates observed protein expression changes with curated activation and inhibition relationships from the IPA knowledge base. A positive z-score indicates a pathway predicted to be activated, while a negative z-score suggests inhibition. Pathways with $|z| \geq 2$ were considered to have strong predictive directionality. Pathways lacking sufficient data for z-score calculation were excluded from visual summaries. Visual heatmaps represent these z-scores using color scales centered at zero, with blue indicating suppression and orange indicating activation.

Immunohistochemistry and Quantitative Image Analysis

Immunohistochemical staining was performed using specific antibodies against angiotensinogen, the precursor of angiotensin, C-Myc, EGFR, IGF1/IGF2, NKX2.3, NR4A3 (NOR-1), PGC-1α (PPARGC1A), PTGES, RETN (Resistin), RUNX2, SRC, STAT1, and phospho-STAT3 (Tyr705) to evaluate protein expression in graft tissues. All antibodies were validated for FFPE human tissues, and staining was conducted according to the manufacturers' protocols, with minor optimizations for antigen retrieval and

detection conditions.

Endothelial and Vascular Marker Staining

Immunohistochemistry was performed using antibodies against CD31, α-smooth muscle actin (αSMA), and endothelial nitric oxide synthase. All stained slides were digitized using a whole-slide scanner (Aperio GT450 DX, Leica Biosystems), and image analysis was conducted using QuPath (v0.5.1). Detailed information on antibody sources, catalog numbers, clones, and working dilutions is provided in Table S2.

eNOS Signal Quantification in Endothelial Cells

Using the area annotation tool in QuPath, the innermost luminal layer was manually annotated to select the target area for analysis. Nuclear segmentation was then performed based on the hematoxylin signal. Because stromal cells near the lumen were occasionally included in this segmentation, manual curation was conducted to remove any non-endothelial cells, ensuring that only true endothelial cells were segmented. Specifically, cells exhibiting characteristic hobnail morphology, indicative of true luminal endothelial cells, were retained, while cells located deeper within the stroma were excluded, as shown in Figure S1C-D.

For each nucleus, the mean optical density of the DAB signal for eNOS was measured. A histogram of per-cell eNOS intensity was generated to visualize the distribution. A threshold of 0.2 was applied to distinguish eNOS-positive from eNOS-negative nuclei. The proportion of eNOS-positive endothelial cells was then calculated relative to the total number of segmented endothelial cells.

Quantification of CD31-Positive Neovessels

To assess neovascularization, including vasa vasorum extending from the media to the adventitia, CD31-stained sections were analyzed using a segmentation-based approach in QuPath. The parameters included a spatial resolution of 0.51 μm/pixel, a Gaussian filter value of 2, an intensity threshold of 0.44, and object/hole size thresholds of 20 pixels. This pipeline enabled consistent detection of small capillaries (Figure S1E–H). Quantification metrics included the total capillary area and the cumulative perimeter of CD31-positive structures.

Digital Quantification of IHC Using QuPath

Immunohistochemical signals were quantified on whole-slide images using QuPath (v0.5.1). For each slide, regions of interest (ROIs) were manually annotated to include representative lesional areas while excluding artifacts. Stain vectors (hematoxylin and DAB) were calibrated on the same slide prior to analysis. Nuclei were segmented using the "Positive cell detection" workflow, with nuclear DAB optical density (OD) serving as the scoring compartment. Intensity thresholds were established to classify cells into 0, 1+, 2+, and 3+ categories consistently across slides for each antibody. Measurements were exported at the annotation level.

For each ROI, the positive percentage was calculated as (#1+ + #2+ + #3+) divided by the total number of nuclei, multiplied by 100. The H-score[1] was computed on a scale ranging from 0 to 300. All thresholding and post-processing parameters were kept constant within each marker to ensure comparability across study groups.

Statistical Analysis

All statistical analyses were conducted using R (v3.2.3; R Foundation for Statistical

Computing). Group comparisons were performed using analysis of variance (ANOVA). To account for repeated measures and inter-individual variability, generalized estimating equations (GEE) were applied, implemented via the geeglm function in the geepack package. Post hoc pairwise comparisons were adjusted using Tukey's method, with Bonferroni correction applied to control for multiple testing.

Raw data from QuPath analysis were imported and processed using Python 3.8 with pandas (version 1.5.3) for data manipulation. A total of 12 proteins were analyzed: angiotensinogen, c-MYC, EGFR, IGF1, NR4A3, PTGES, PGC, RETN, RUNX2, SRC, STAT1, and STAT3.

Quantitative immunohistochemical data were analyzed using non-parametric statistical methods due to the data's non-normal distribution. For each protein, two primary outcome measures were evaluated: the percentage of positive cells (Positive %) and the H-score, both derived from QuPath analysis software. Statistical significance was set at $\alpha=0.05$.

Results were visualized using box-and-whisker plots combined with individual data point overlays (swarm plots) to illustrate both distribution characteristics and individual observations. The plots were generated using the Matplotlib (version 3.7.1) and Seaborn (version 0.12.2) libraries, adhering to academic formatting standards suitable for publication. Statistical significance was indicated on the plots with horizontal lines and asterisk notation above the compared groups.

SUPPLEMENTAL RESULTS

Histomorphological Characteristics of Patent Arterial and Venous Grafts (continued)

Native arterial conduits, freshly harvested for CABG (AC), exhibited the expected features of elastic arteries, including a compact medial layer rich in elastic fibers and well-defined internal and external elastic laminae. After grafting, AGP retained this elastic-artery framework but showed reinforcement of the internal elastic lamina and marked thickening of the muscular media, with minimal intimal hyperplasia—findings consistent with stable structural adaptation. Native venous conduits, freshly harvested for CABG (VC), exhibited thin vessel walls, wide lumina, sparse medial elastic fibers, and an indistinct elastic laminar structure.

Quantitative morphometric analysis revealed distinct graft-type–specific patterns in vessel dimensions (Figure 1C). Lumen area showed minimal differences between AGP and their native AC. VGP exhibited a modest reduction in lumen area compared with VC, resulting in lumen dimensions that approached those of AGP—reflecting the extent to which the venous conduit had remodeled toward the size range of an arterial conduit. In contrast, VGO showed a pronounced increase in lumen area ($P<0.001$), consistent with the aneurysmal dilatation observed histologically. A similar pattern was observed in lumen circumference, with VGO demonstrating substantial enlargement relative to all other groups.

Intimal measurements revealed mild thickening in AGP compared with AC ($P<0.001$), indicating neointimal growth in arterial grafts. VGO showed a markedly enlarged intimal area compared with VGP ($P<0.001$), consistent with the severe structural distortion observed in failed grafts. Medial thickness was significantly greater in AGP than in AC ($P<0.001$), reflecting adaptive medial hypertrophy. VGP showed a non-significant trend

toward increased medial thickness relative to VC. Conversely, VGO exhibited a significant reduction in medial thickness compared with both VGP and VC ($P<0.001$), indicating medial degeneration associated with graft failure.

Intimal and Medial Morphology Across Arterial and Venous Graft States (Figure 1D)

In AGP, intimal changes were minimal compared with native AC. AGP showed a well-preserved luminal surface without cleft formation, a more prominent internal elastic lamina, and reduced elastic fiber content within the media—features indicative of a shift from an elastic artery pattern toward a more muscular artery configuration.

VGP exhibited substantial intimal thickening compared with native VC. The intima of VGP contained interspersed clefts and internal striations, accompanied by a markedly thickened internal elastic lamina. The media showed increased elastic fiber deposition along with smooth muscle hypertrophy, indicating progressive structural remodeling in response to arterial hemodynamic stress. In contrast, VGO exhibited a distinctly different pattern. The intimal surface was smooth and rounded, lacking clefts, and was composed predominantly of dense, disorganized collagen. The endothelial lining was absent, and luminal calcification was frequently observed. The media showed extensive necrosis and loss of normal elastic laminar structures. These findings highlight that, although both VGP and VGO develop intimal thickening, the underlying organization and associated medial changes differ profoundly between patent and failed grafts.

Robust Proteomic Profiling of Archival Graft Tissue

To evaluate protein expression signatures across graft types, we performed label-free quantitative proteomics on FFPE vascular grafts. Across all 26 samples, an average of over

3,000 proteins were confidently identified per sample (Figure S2). Quantile-based normalization (Q1–Q3) of protein abundance resulted in tightly aligned $\log_2$ distributions, minimizing systematic bias and enhancing cross-sample comparability. Following normalization, protein abundance profiles exhibited nearly identical ranges and medians across groups. Technical reproducibility was confirmed by Pearson correlation analysis, which revealed strong within-group clustering and high concordance between biological replicates (Figure S2).

A total of 4,836 proteins were identified across all vascular samples. Among these, 4,012 proteins were shared across all five groups, representing a substantial common vascular proteome (Figure S3).

Sparse Partial Least Squares Discriminant Analysis

To show group separation, we performed sPLS-DA (Figure S3B). Consistent with the PCA findings, AGP and VGP showed close proximity, whereas VGO remained distinctly segregated from all other groups. To identify discriminative molecular features, we examined the loading profiles. The highest-ranked contributors on Component 1 included glycolytic enzymes, cytoskeletal regulators, and stress-associated proteins.

The three-dimensional plot showed that both AGP and VGP clustered distinctly from their respective controls, indicating convergent remodeling signatures under arterial hemodynamic stress. In contrast, VGO samples formed a separate cluster, distinct from both VGP and VC, reflecting a proteomic profile consistent with maladaptive or fibro-inflammatory remodeling.

Examination of the loading vectors identified the proteins most strongly contributing to Component 1. High VIP scores were observed for proteins that regulate glycolysis,

cytoskeletal stability, and mitochondrial protein homeostasis, which were consistently elevated in functional grafts (AGP and VGP), reflecting active metabolic remodeling and preservation of structural integrity under arterial hemodynamic stress.

Component 2 captured vein-specific remodeling features driven by extracellular matrix and mitochondrial regulatory proteins. These proteins were enriched in VGO relative to AGP/VGP, indicating enhanced ECM deposition, altered mitochondrial signaling, and immune-activated remodeling characteristic of graft failure.

Divergent Baseline Proteomic Programs in Native Arteries and Veins (Clusters 6 and 7)

Unsupervised hierarchical clustering identified two native vessel–specific clusters, corresponding to Cluster 6 (AC) and Cluster 7 (VC). Pathway enrichment analysis (Figure S4A) revealed that Cluster 6 (AC) was enriched in biological processes related to epithelial differentiation, keratinization, and intermediate filament organization. In contrast, Cluster 7 (VC) showed preferential enrichment of pathways associated with vascular smooth muscle contraction, actin cytoskeleton remodeling, and extracellular matrix interactions. PPI network analysis (Figure S4B) further supported these distinctions: AC networks were dominated by keratin family members, laminins, and collagens, whereas VC networks centered on actomyosin contractile proteins. Metascape enrichment bubble plots (Figure S4C) highlighted these contrasting themes, with AC associated with structural reinforcement and barrier-related programs, and VC linked to cytoskeletal plasticity, cell–matrix adhesion, and vascular repair pathways. Together, these findings reinforce the baseline molecular divergence between native arteries and veins and provide a reference framework for interpreting graft-associated remodeling.

Upstream Regulators and Pathway Programs Distinguishing Arterial Grafts from AC

Upstream regulator analysis comparing AGP with native internal AC revealed a coordinated upregulation of multiple metabolic and proliferative regulators (Figure 4A). Key activated upstream nodes included IGF1, RUNX2, NR4A3, PGC-1α, EGFR, and MYC, which converge on biological functions related to cell proliferation, connective tissue growth, and metabolic activation. These regulators formed a coherent signaling network, indicating that arterial grafts engage a distinct adaptive remodeling program absent in control arteries. Consistent with these upstream predictions, AGP demonstrated enrichment of canonical pathways supporting the biosynthetic and metabolic aspects of vascular remodeling (Figures S6–S10). These pathways included those mediating protein quality control and stress adaptation (BAG2 signaling), mitochondrial energy metabolism (oxidative phosphorylation, sirtuin signaling), biosynthetic translational control (mTOR signaling, regulation of eIF4 and p70S6K), autophagy and vesicular turnover (microautophagy signaling), innate immune effector pathways (neutrophil degranulation, nitric oxide and reactive oxygen species production), angiogenic signaling (VEGF pathway), and nutrient stress–responsive translational regulation (signal recognition particle [SRP]–dependent cotranslational targeting, EIF2AK4/GCN2 amino acid deficiency response, EIF2 signaling).

Collectively, these findings show that arterial graft adaptation is characterized by IGF1–RUNX2–driven metabolic and proliferative reprogramming, supported by coordinated activation of mitochondrial, biosynthetic, and immunoregulatory pathways. This integrated signaling architecture defines an adaptive remodeling phenotype distinct from the quiescent state of native arterial conduits.

Activation of Proliferative and Biosynthetic Programs and Suppression of Contractile

Regulators in Patent Vein Grafts (continued)

Pathway-level analyses (Figures S11–S13) further substantiated the findings shown in Figure 4B. VGP demonstrated reduced activity in the GP6 signaling pathway, a collagen receptor cascade, suggesting decreased platelet–extracellular matrix interactions during vein graft adaptation. Concurrent alterations were observed in components of collagen biosynthesis and modifying enzyme networks, reflecting extracellular matrix remodeling associated with vein graft adaptation to arterial hemodynamics. VGP also exhibited enrichment of EIF2 signaling and integrin signaling pathways, indicating activation of translational control and cytoskeletal remodeling programs. Additionally, VGP showed activation of signal recognition particle (SRP)–dependent cotranslational protein targeting, the EIF2AK4/GCN2 amino acid deficiency response, and the integrated stress response. These translational stress-adaptation pathways overlapped with those activated in arterial grafts (AGP vs. AC), suggesting conserved protein synthesis and stress-response programs across both graft types during adaptation to arterial pressure environments.

SUPPLEMENTAL FIGURES

SUPPLEMENTAL FIGURE LEGENDS

Figure S1

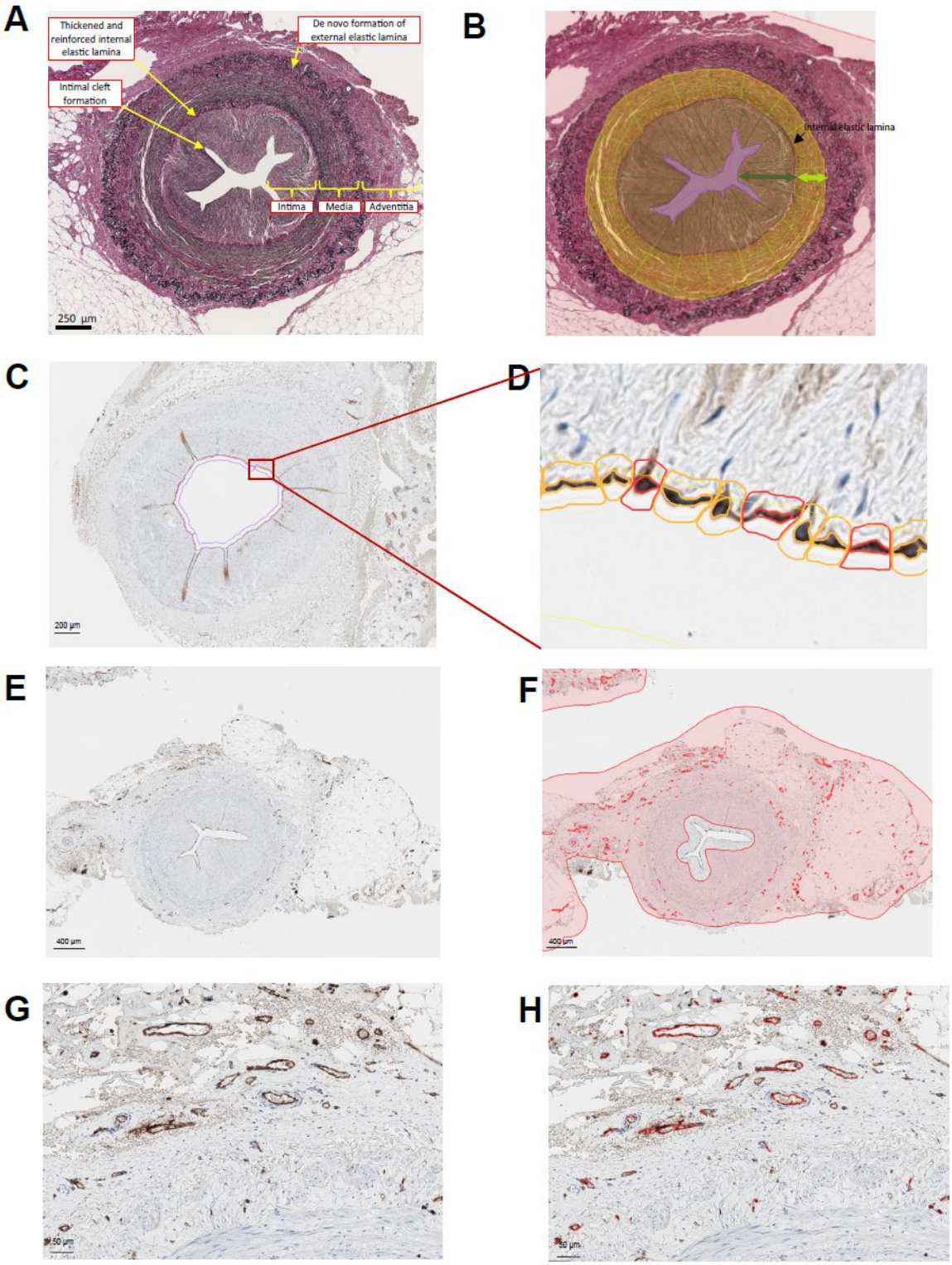

(A) Long-term patent SV graft showing significant intimal hyperplasia and cleft formation

Histomorphological analysis of long-term patent SV grafts revealed intimal hyperplasia, cleft formation, and increased eNOS expression in the luminal endothelium and adventitial vasa vasorum.

(B) Digitally scanned images were analyzed using QuPath with manual annotation and quantification. The lumen area (L, purple line) was measured by delineating the innermost lumen perimeter. Intimal thickness (I, green arrow) was defined as the distance between the internal elastic lamina (IEL, black line) and the main lumen, while medial thickness (M, light green arrow) was measured as the distance between the IEL and the outer border of the medial smooth muscle layer. Cleft depth (magenta line) was defined as the distance from a virtual line smoothing the main lumen to the deepest part of the cleft.

(C-D) Digital image analysis workflow for quantifying luminal eNOS. C, Representative eNOS immunohistochemistry with annotated luminal endothelium (pink outline). Scale bar=200 μm. D, High-magnification view demonstrating QuPath-based nuclear segmentation (hematoxylin, blue) and cell boundary detection (orange/red outlines). Mean DAB optical density was quantified for each nucleus across 20,792 endothelial cells for single-cell distribution analysis (Figure 6B).

(E-H) Quantification of adventitial CD31-positive capillaries. Whole-section view showing CD31-positive vasa vasorum. Scale bar=400 μm. D, Annotation of the media-adventitial compartment (pink) for selective microvessel analysis, excluding the luminal endothelium. Scale bar=400 μm.

(G-H) High-magnification view of CD31-positive adventitial neovascularization in a patent saphenous vein graft. Scale bar=50 μm. F, QuPath segmentation of CD31-positive vessels

(red outlines) for automated perimeter quantification (Figure 6E, left). Scale bar=50 µm.

All sections were digitized at 20× magnification. QuPath (v0.4.3) parameters included a nuclear diameter of 5–15 µm, cytoplasmic expansion of 2 µm, and DAB color deconvolution using standard vectors. The eNOS positivity threshold was defined as an optical density greater than 0.2.

Figure S2. Robust proteomic profiling of archival vascular graft tissue

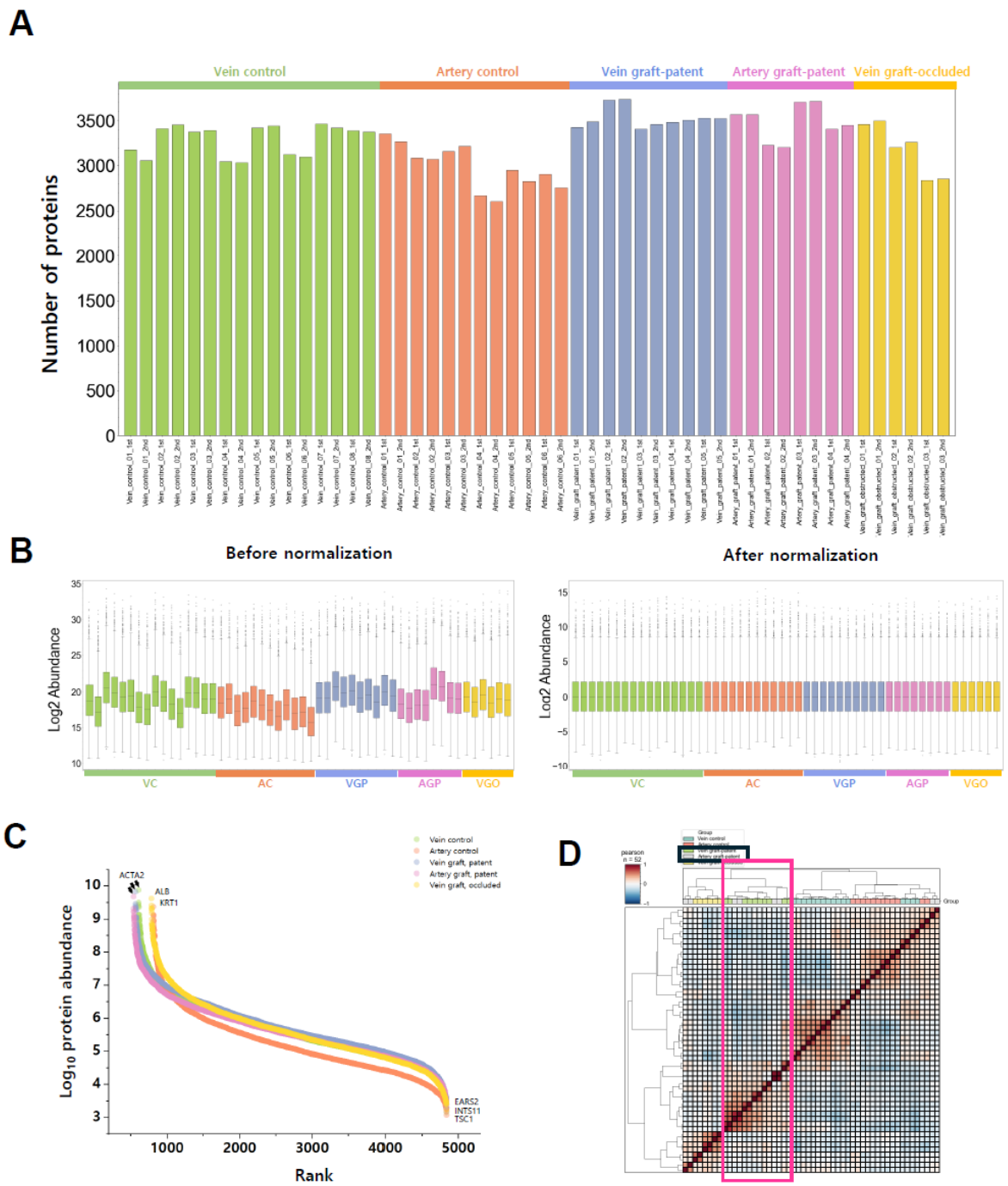

(A) Number of identified proteins. Bar plot showing the total number of confidently identified proteins per sample across all graft categories. Despite the archival formalin-fixed, paraffin-embedded nature of the tissues, each sample yielded high-depth proteomic coverage, with an average of over 3,000 proteins identified.

(B) Distribution of sample abundance. Distribution of $\log_2$-transformed protein abundance values before (left) and after (right) quantile-based normalization (Q1–Q3). Each box plot represents individual samples grouped by vessel type: VC (native vein controls), AC (native arterial controls), VGP (patent venous grafts), AGP (patent arterial grafts), and VGO (occluded venous grafts).

Before normalization, substantial systematic variability is evident across groups, characterized by differing medians and dynamic ranges. After normalization, the distributions were aligned, exhibiting comparable medians and interquartile ranges across all groups; this process minimizes technical bias while preserving biological differences. The normalization method employed was asymmetric quartile-based scaling, in which the median (Q2) was subtracted from all values to center each distribution; values above the median were scaled by (Q3 − Q2), and values below the median were scaled by (Q2 − Q1).

(C) Ranked protein abundance. Rank–abundance plots demonstrating consistent detection of highly abundant vascular structural proteins, including ACTA2, KRT1, and albumin, across all samples and graft types.

(D) Pearson correlation heatmap revealed strong within-group clustering and high concordance between biological replicates, confirming the robust technical reproducibility of the proteomic dataset.

Figure S3

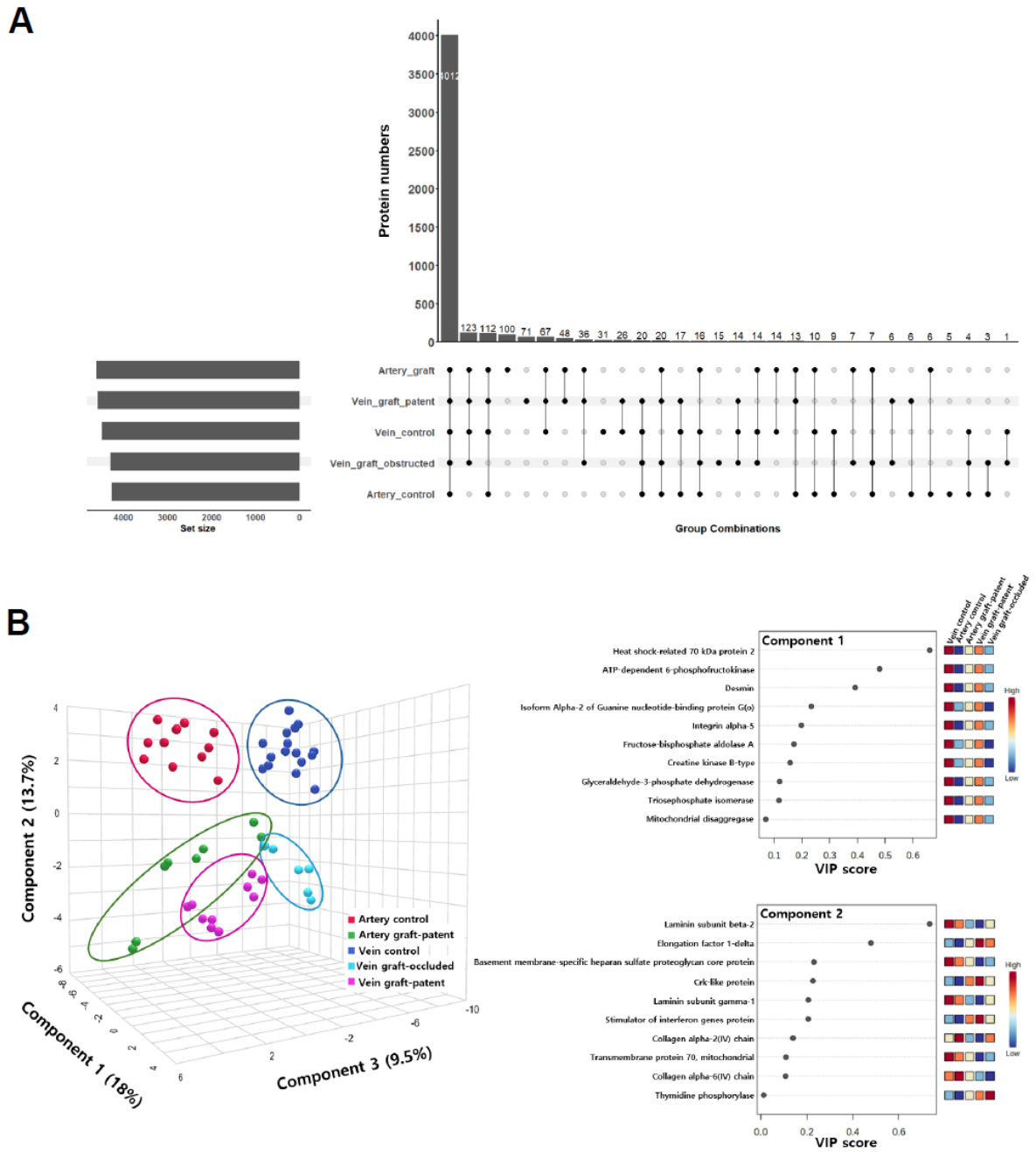

(A) Intersection analysis of detected proteins across vascular groups using the ComplexUpset package (v1.3.3). A total of 4,836 proteins were identified across all samples. The bar plot on the left displays the number of detected proteins within each group (AC, VC, AGP, VGP, VGO), demonstrating comparable proteomic depth across the datasets. The intersection

matrix and the accompanying bar plot illustrate the shared and unique protein sets among the five groups, with 4,012 proteins commonly detected across all groups. Each group also exhibits a subset of uniquely detected proteins, indicating condition-specific proteomic features that distinguish native vessels, patent grafts, and occluded grafts.

(B) sPLS-DA clustering and discriminant protein loadings. (Left) 3D sPLS-DA score plot (Components 1–3) illustrating the separation among native vessels (AC, VC), patent grafts (AGP, VGP), and occluded grafts (VGO). AGP and VGP showed partial overlap, whereas VGO formed a discrete cluster. (Right) Loading plots for Components 1 and 2, highlighting proteins with the greatest contribution to group discrimination. The top-ranked contributors include glycolytic enzymes (PFKP, ALDOA, GAPDH), cytoskeletal proteins (DES, ITGA5), and stress-associated markers (HSPA2, CKB).

Figure S4. Baseline proteomic signatures of native arteries and veins (Clusters 6 and 7).

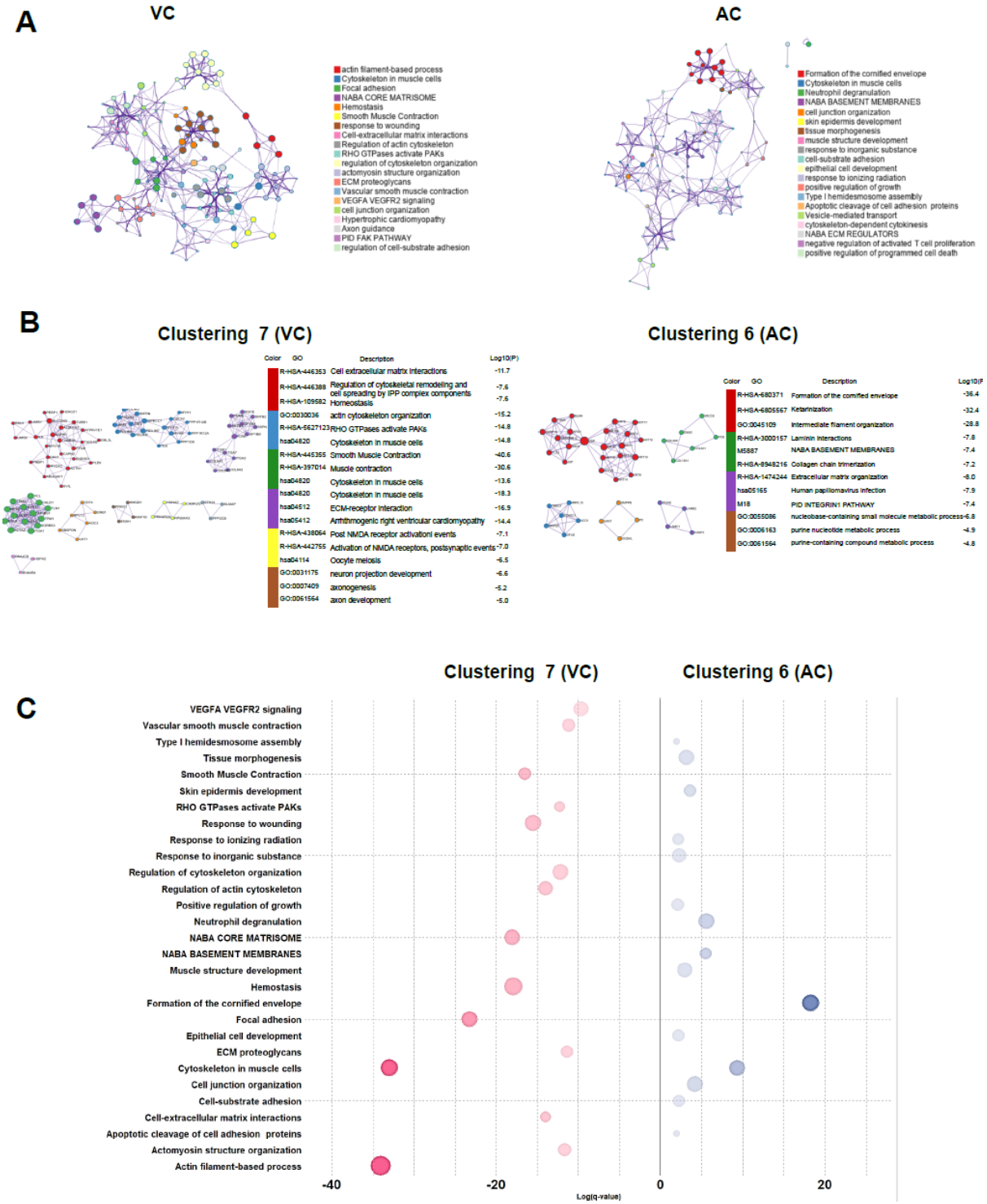

(A) PPI network maps for Cluster 6 (AC) and Cluster 7 (VC), illustrating distinct interaction modules and dominant protein groups within each native vessel cluster.

(B) Metascape functional enrichment networks showing major biological processes represented in Cluster 6 and Cluster 7.

(C) Metascape enrichment bubble plots (GO/KEGG/Reactome) highlighting the top enriched pathways for each cluster. Cluster 6 (AC) was enriched for epithelial differentiation, keratinization, and intermediate filament organization, whereas Cluster 7 (VC) was enriched for vascular smooth muscle contraction, actin cytoskeleton remodeling, and ECM-associated processes. These analyses confirm the divergent baseline proteomic programs of arteries and veins, providing a reference framework for interpreting graft-associated remodeling.

Figure S5. Protein–protein interaction (PPI) networks for Cluster 5.

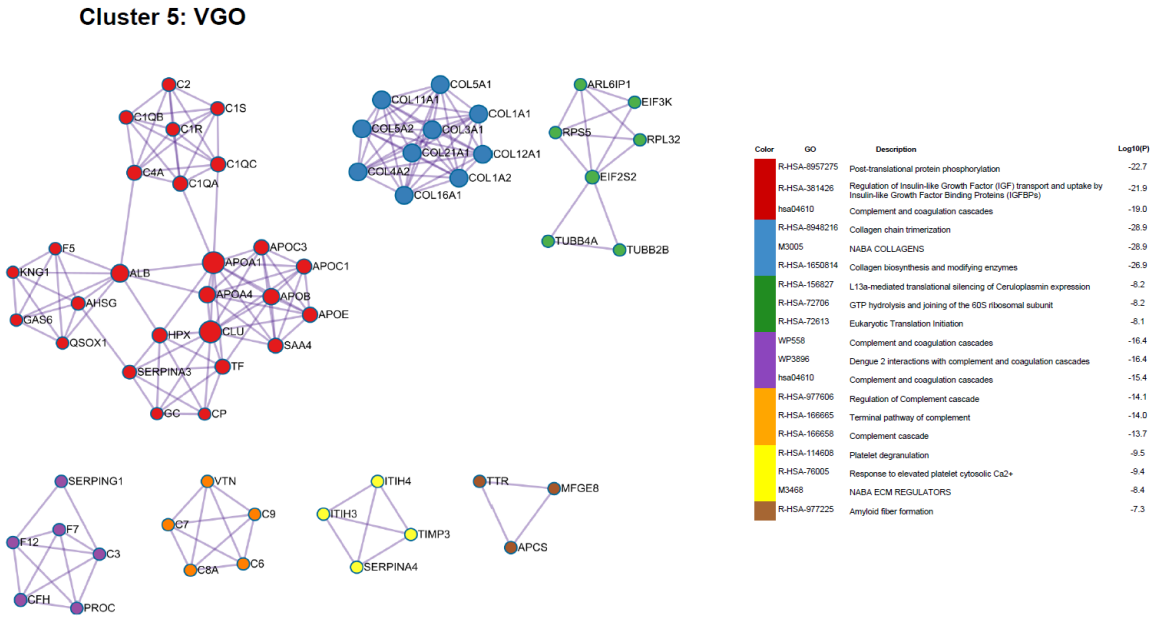

Cluster 5 PPI networks formed extensive complement and coagulation clusters, indicative of a maladaptive and pro-thrombotic remodeling program.

Figure S6. IPA canonical pathway maps highlighting BAG2 signaling, oxidative phosphorylation, and sirtuin signaling in arterial grafts (AGP vs. AC).

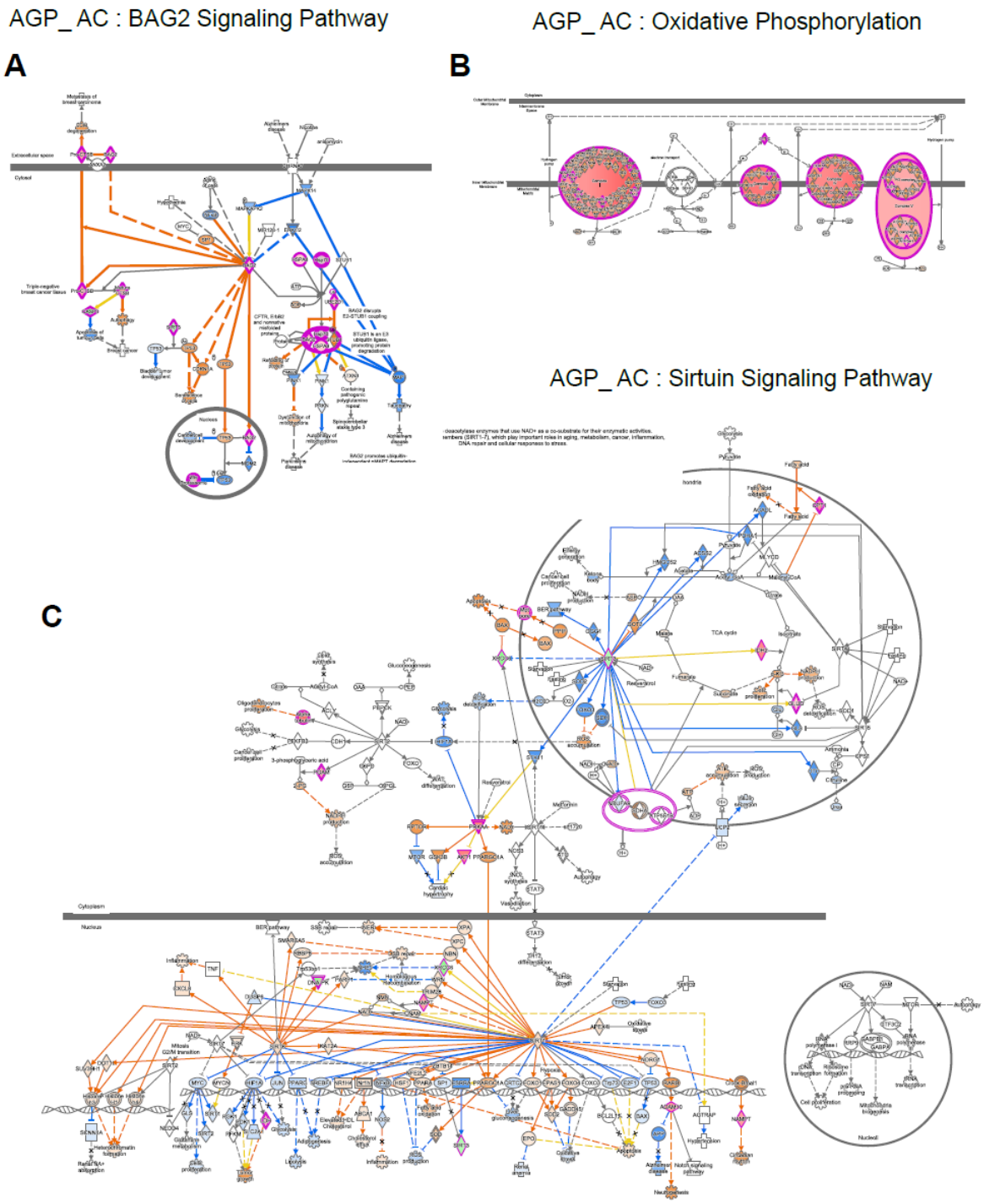

(A) BAG2 signaling pathway. Ingenuity Pathway Analysis (IPA) canonical pathway diagram showing upregulated components (magenta) involved in BAG2-mediated chaperone

regulation and proteostasis in AGP relative to AC. The predicted activation flow (orange arrows) indicates enhanced protein quality control and chaperone-dependent degradation signaling.

(B) Oxidative phosphorylation. Canonical pathway map illustrating the increased representation of mitochondrial respiratory chain components in AGP. Highlighted nodes (magenta) correspond to complexes involved in electron transport and ATP production, consistent with the elevated mitochondrial oxidative capacity observed in arterial grafts.

(C) Sirtuin signaling pathway. IPA pathway diagram demonstrating the differential activation of sirtuin-associated metabolic and stress-response modules in AGP. Upregulated nodes (magenta) and predicted activation steps (orange and blue arrows) reflect enhanced mitochondrial metabolism, redox homeostasis, and NAD^+-dependent regulatory signaling in grafted arterial tissue.

Figure S7. IPA canonical pathway maps highlighting mTOR signaling and translational control in arterial grafts (AGP vs. AC).

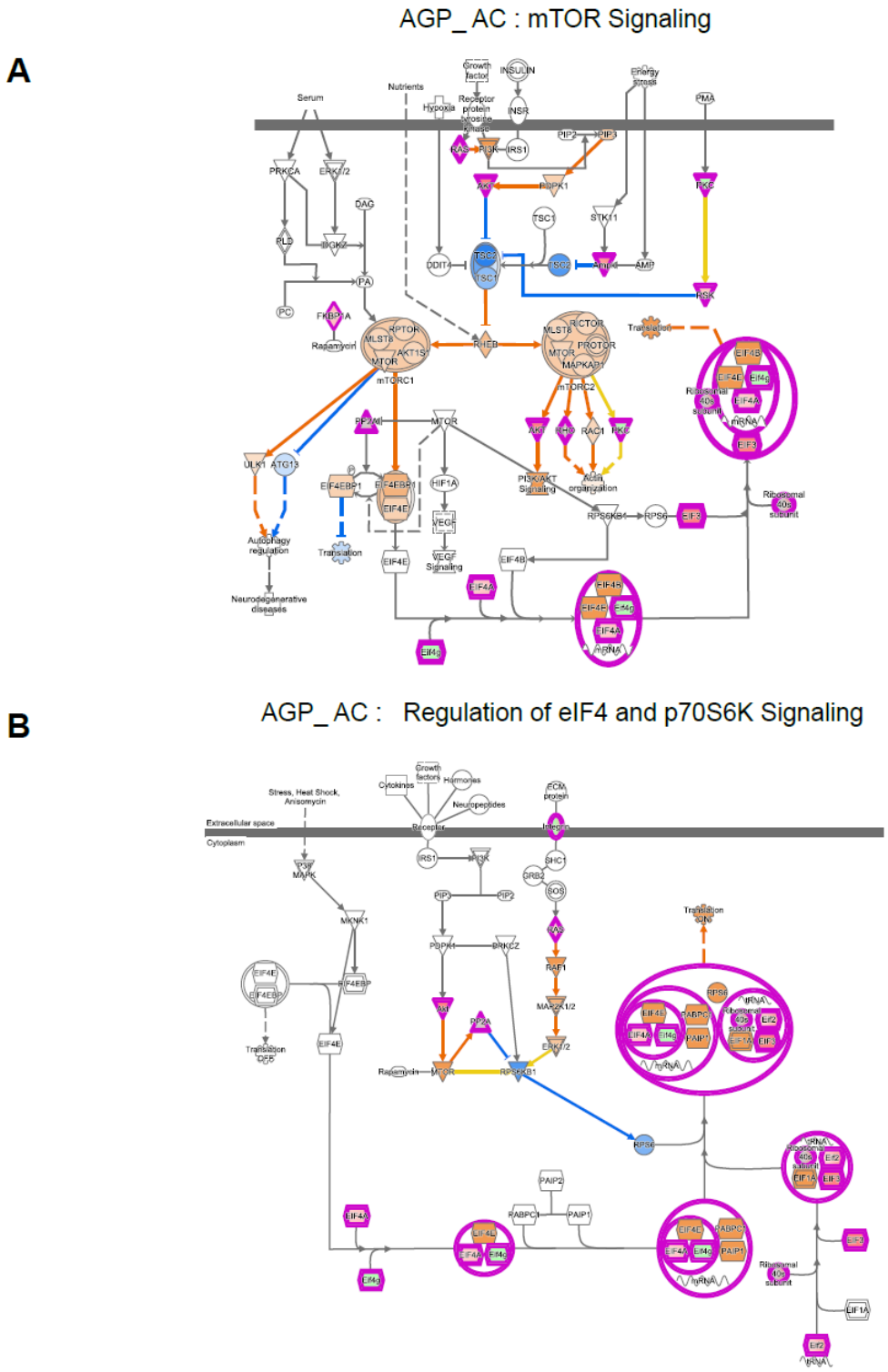

(A) mTOR Signaling. Ingenuity Pathway Analysis (IPA) canonical pathway diagram showing

differential activation of mTORC1- and mTORC2-associated modules in AGP relative to AC. Upregulated nodes (highlighted in magenta) and predicted activation flow (orange arrows) reflect enhanced nutrient- and growth factor–responsive signaling, including the downstream regulation of protein synthesis, autophagy, and cytoskeletal organization.

(B) Regulation of eIF4 and p70S6K Signaling. Canonical pathway map illustrating the upregulation of translation initiation machinery and ribosomal protein activation in AGP versus AC. Highlighted nodes (magenta) and predicted activation steps (orange arrows) indicate increased eIF4 complex activity, p70S6K signaling, and translational output, consistent with the elevated biosynthetic demand in arterial grafts.

Figure S8. IPA canonical pathway maps illustrating microautophagy signaling and neutrophil degranulation in arterial grafts (AGP vs. AC).

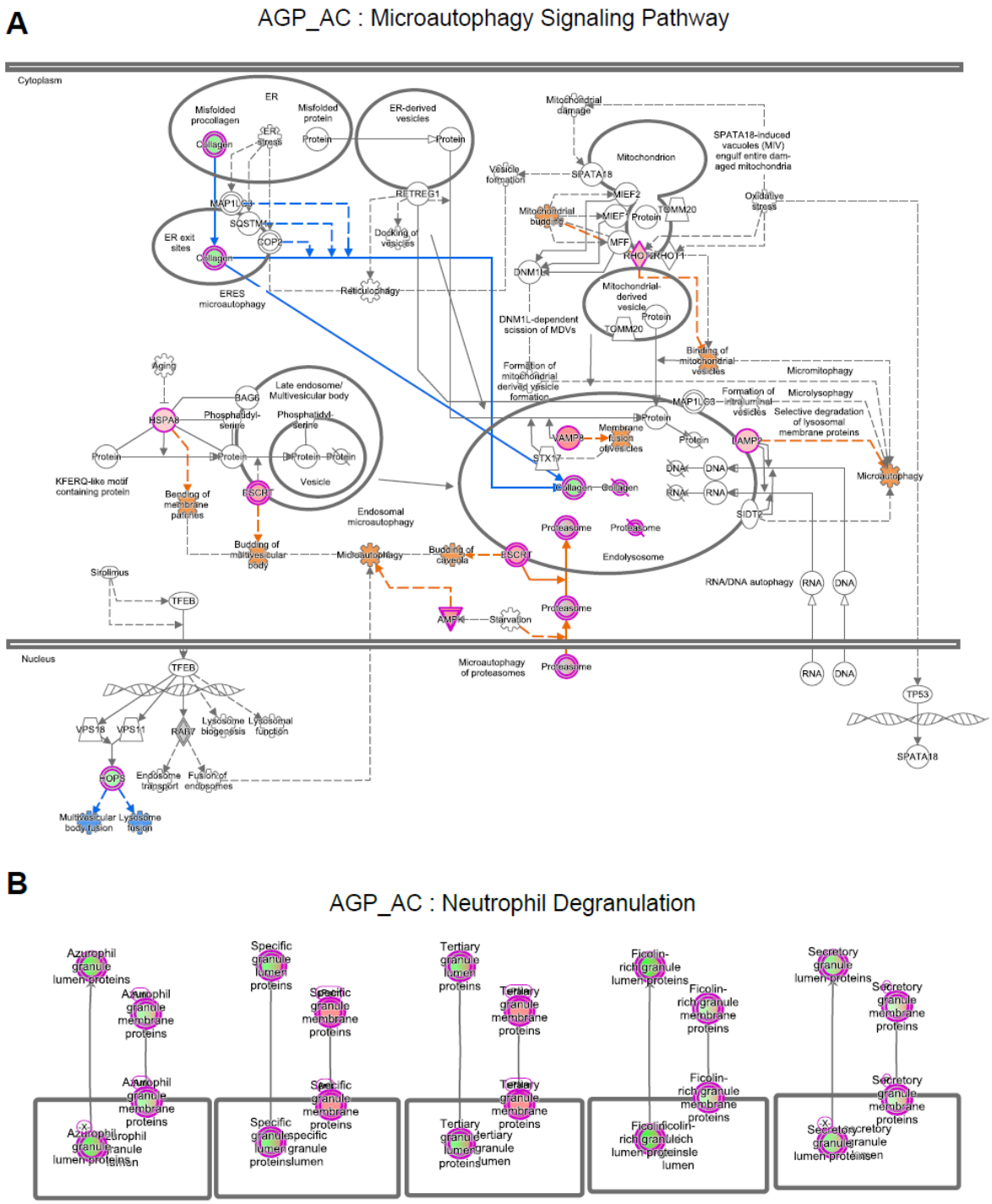

(A) Microautophagy Signaling Pathway. Ingenuity Pathway Analysis (IPA) canonical pathway diagram showing upregulated components (highlighted in magenta) involved in ER-

derived vesicle formation, endosomal and lysosomal trafficking, mitophagy-related processes, and microautophagy-associated protein turnover in AGP relative to AC. Predicted activation flows (orange arrows) reflect enhanced autophagy-linked proteostasis mechanisms in arterial grafts.

(B) Neutrophil Degranulation. Canonical pathway map depicting proteins associated with azurophilic, specific, tertiary, and secretory granule compartments. Highlighted nodes (magenta) represent granule-associated proteins upregulated in AGP compared with AC, indicating enhanced neutrophil degranulation–related signatures within the arterial graft microenvironment.

Figure S9. IPA canonical pathway maps highlighting nitric oxide/ROS production and VEGF signaling in arterial grafts (AGP vs. AC).

A AGP_AC : Production of Nitric Oxide and Reactive Oxygen Species in Macrophages

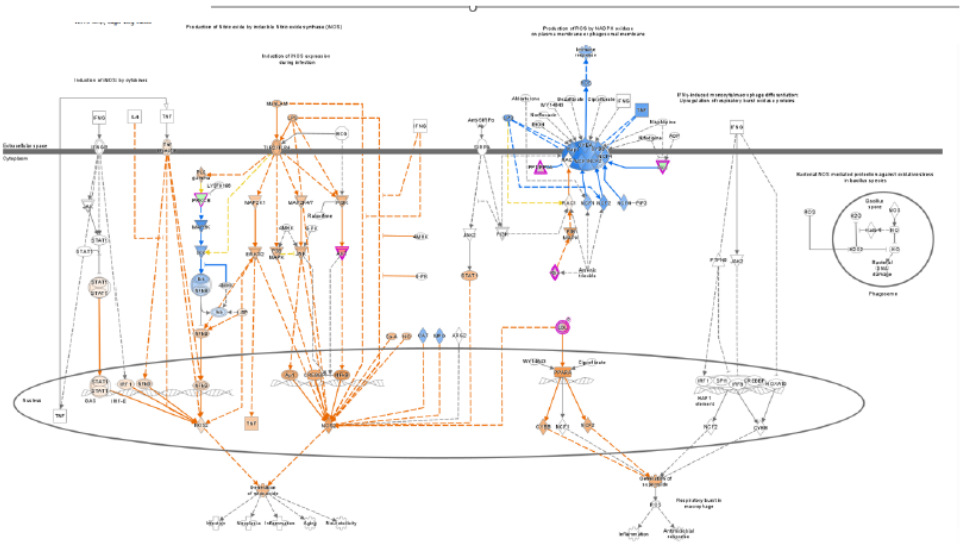

B AGP_AC : VEGF Signaling

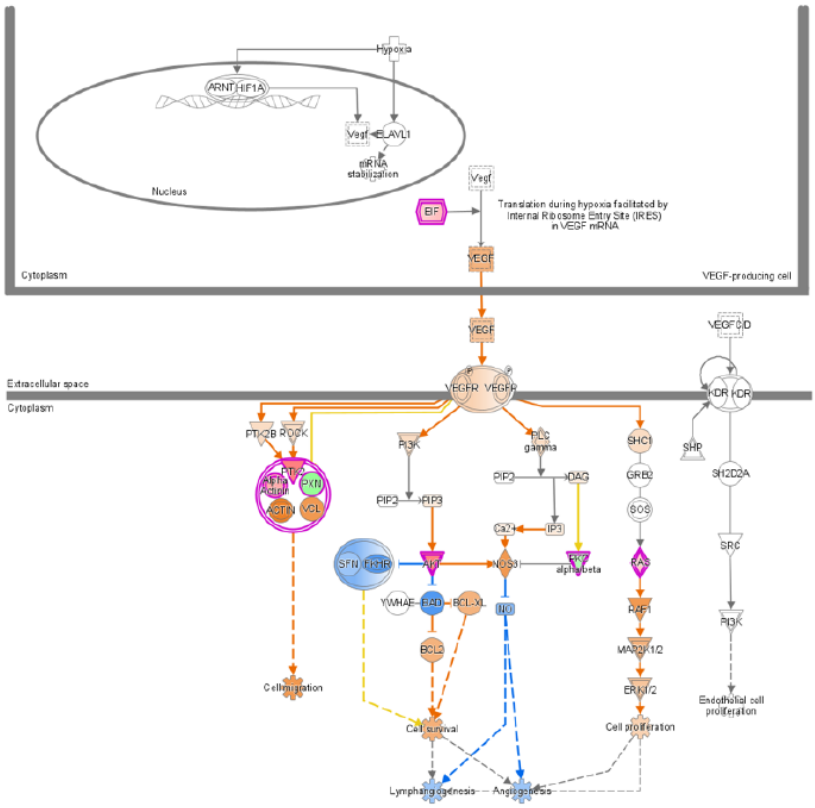

(A) Production of Nitric Oxide and Reactive Oxygen Species in Macrophages. Ingenuity

Pathway Analysis (IPA) canonical pathway diagram showing differential activation of nitric oxide– and reactive oxygen species–related signaling components in AGP relative to AC. Upregulated nodes (highlighted in magenta) and predicted activation flow (orange arrows) illustrate enhanced redox-associated signaling in arterial grafts.

(B) VEGF Signaling. Canonical pathway map depicting VEGF signaling in the AGP vs. AC comparison. Highlighted nodes (magenta) and predicted activation pathways (orange arrows) reflect enhanced VEGF receptor–mediated signaling, including downstream PI3K/AKT, MAPK/ERK, and endothelial survival/migration pathways.

Figure S10. IPA canonical pathway maps highlighting translational and stress-response signaling in arterial grafts (AGP vs. AC).

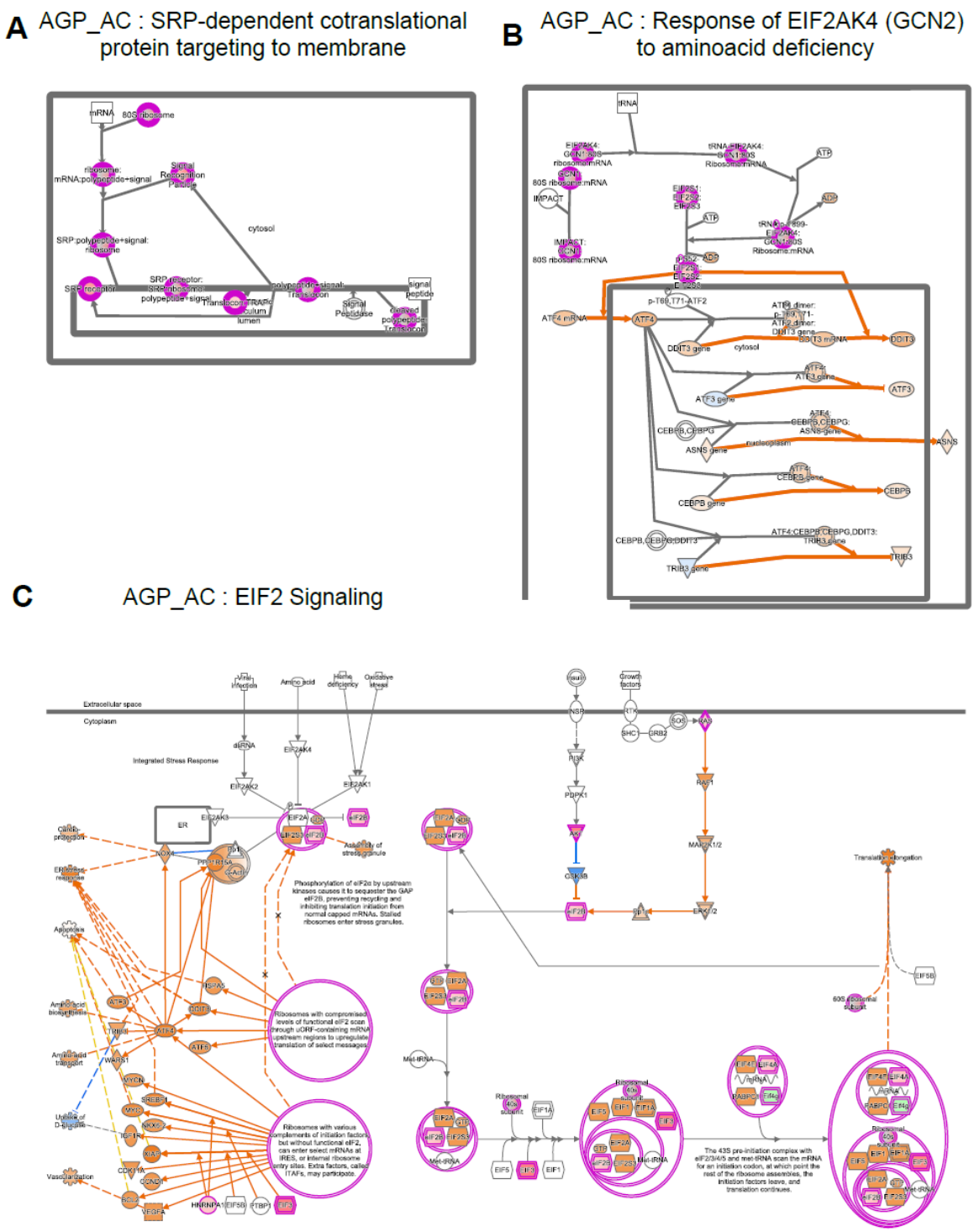

(A) SRP-dependent cotranslational targeting of proteins to the membrane. Ingenuity Pathway

Analysis (IPA) canonical pathway diagram showing upregulated components (magenta) in AGP relative to AC, indicating enhanced engagement of ribosome–SRP complexes and ER-directed cotranslational processing.

(B) Response of EIF2AK4 (GCN2) to amino acid deficiency. Canonical pathway map illustrating the activation of the GCN2–ATF4 axis in AGP. Upregulated nodes (magenta) and predicted activation flow (orange arrows) highlight enhanced amino acid sensing and downstream integrated stress response gene activation.

(C) EIF2 signaling. Pathway diagram illustrating the broad activation of EIF2 signaling in AGP, including upregulated translation initiation factors, ribosomal proteins, and ATF-dependent stress-response modules. Predicted activation (orange arrows) and highlighted nodes (magenta) reflect increased translational demand and ISR engagement in arterial grafts.

Figure S11. IPA canonical pathway maps illustrating extracellular matrix remodeling and platelet-related signaling in functional vein grafts (VGP vs. VC).

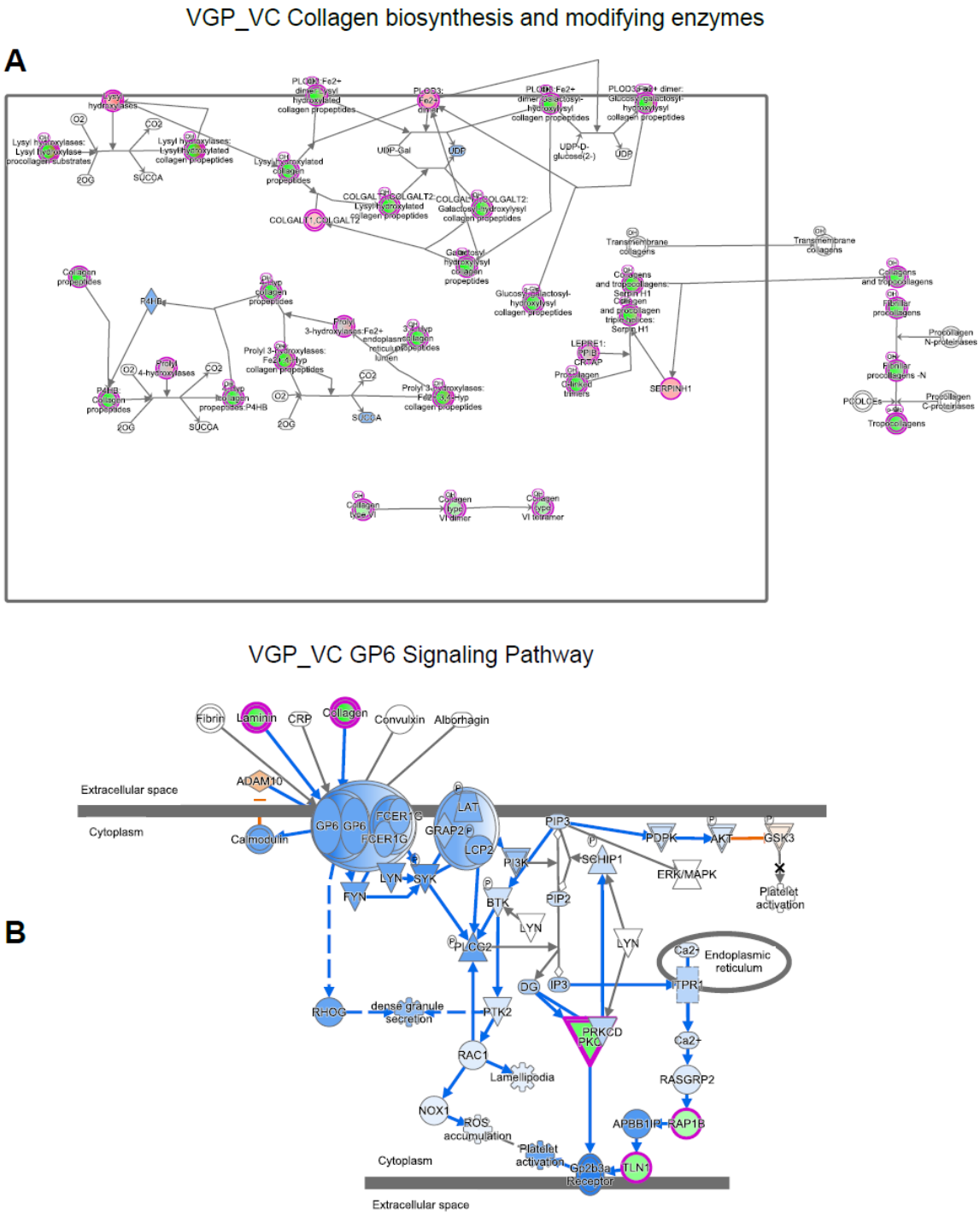

(A) Collagen biosynthesis and modifying enzymes. Ingenuity Pathway Analysis (IPA) canonical pathway map showing upregulated components (magenta) involved in collagen

chain synthesis, hydroxylation, glycosylation, cross-linking enzymes (e.g., LOX family), and procollagen processing in VGP relative to VC. These enriched nodes highlight enhanced extracellular matrix production and collagen maturation in functional vein grafts.

(B) GP6 signaling pathway. IPA canonical pathway map for GP6 signaling demonstrating altered platelet-related signaling events in the VGP vs. VC comparison. Upregulated nodes (magenta) and predicted activations (blue/orange arrows depending on pathway direction) indicate changes in collagen–platelet interaction modules, downstream cytoskeletal rearrangements, and platelet activation signaling.

Figure S12. IPA canonical pathway maps highlighting EIF2 signaling and integrin signaling in functional vein grafts (VGP vs. VC).

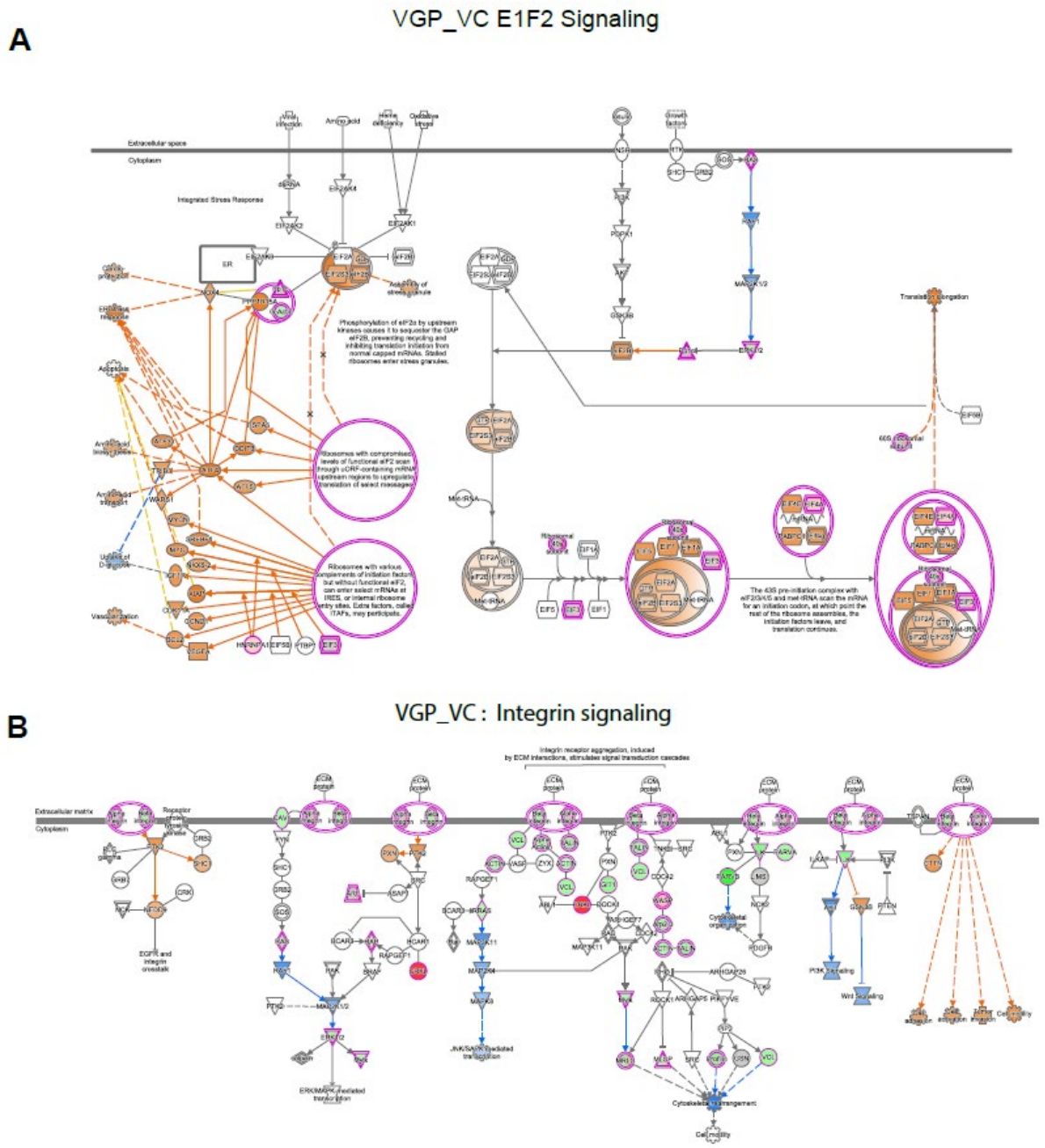

(A) EIF2 signaling. Ingenuity Pathway Analysis (IPA) canonical pathway map illustrating the EIF2 signaling cascade in the VGP vs. VC comparison. Upregulated components (highlighted in magenta) indicate activation of the integrated stress response, including increased EIF2

phosphorylation, ATF4-driven transcriptional programs, and downstream stress-adaptation modules. Predicted pathway activation is shown by orange arrows.

(B) Integrin signaling. IPA canonical pathway map for integrin signaling in VGP vs. VC. Highlighted nodes (magenta) demonstrate upregulation of focal adhesion components, integrin receptor complexes, cytoskeletal regulators, and downstream MAPK/JNK-mediated signaling events. These findings are consistent with enhanced adhesion, mechanotransduction, and cytoskeletal remodeling in functional grafts.

Figure S13. Canonical pathway maps illustrating translational and stress-response programs enriched in functional vein grafts (VGP vs. VC).

A VGP_VC SRP-dependent cotranslational protein targeting to membrane

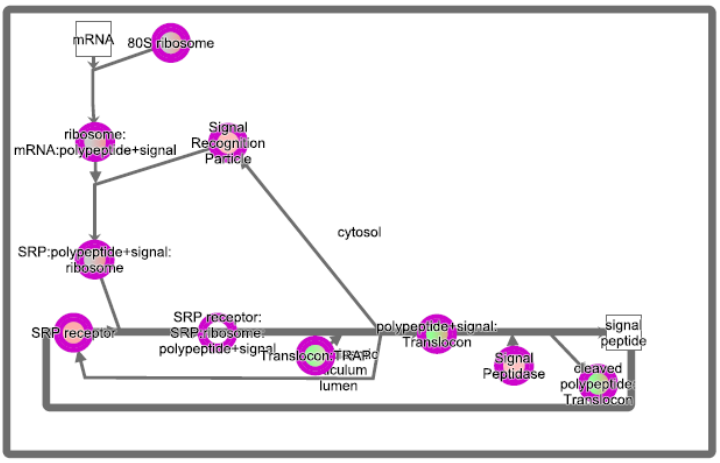

B VGP_VC : Response of EIF2AK4 (GCN2) to aminoacid deficiency

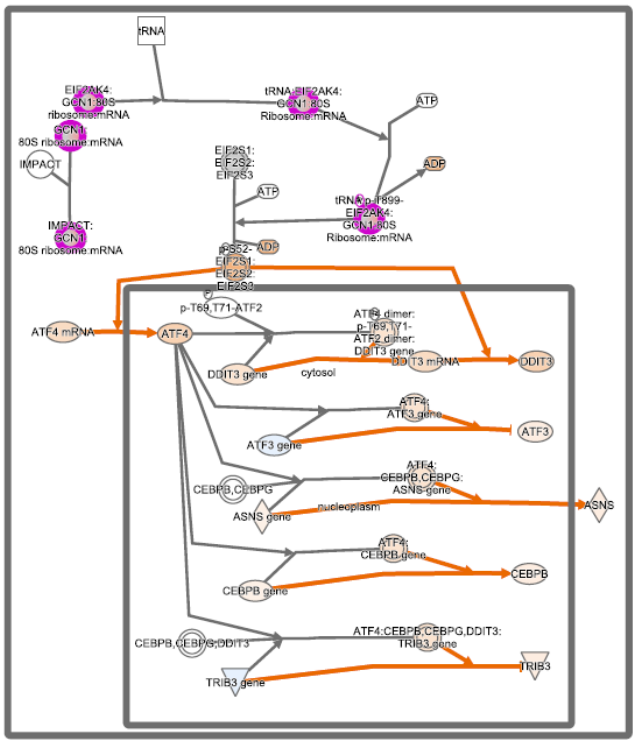

(A) IPA canonical pathway diagram for the *SRP-dependent cotranslational protein targeting to the membrane*, highlighting upregulated components (magenta) in VGP relative to VC.

This pathway represents increased engagement of ribosome–SRP complexes and endoplasmic reticulum translocation machinery, consistent with enhanced cotranslational processing in functional grafts.

(B) IPA canonical pathway diagram for the *Response of EIF2AK4 (GCN2) to amino acid deficiency*, showing activation of GCN2-ATF4–dependent stress adaptation modules in VGP. Upregulated nodes (magenta) and predicted activation flow (orange arrows) indicate enhanced amino acid sensing, integrated stress response signaling, and downstream transcriptional activation. These pathway maps summarize the key translational and stress-adaptive mechanisms identified in the VGP vs. VC comparison.

Figure S14. Immunohistochemical assessment of PGC-1α and c-Myc expression across graft conditions.

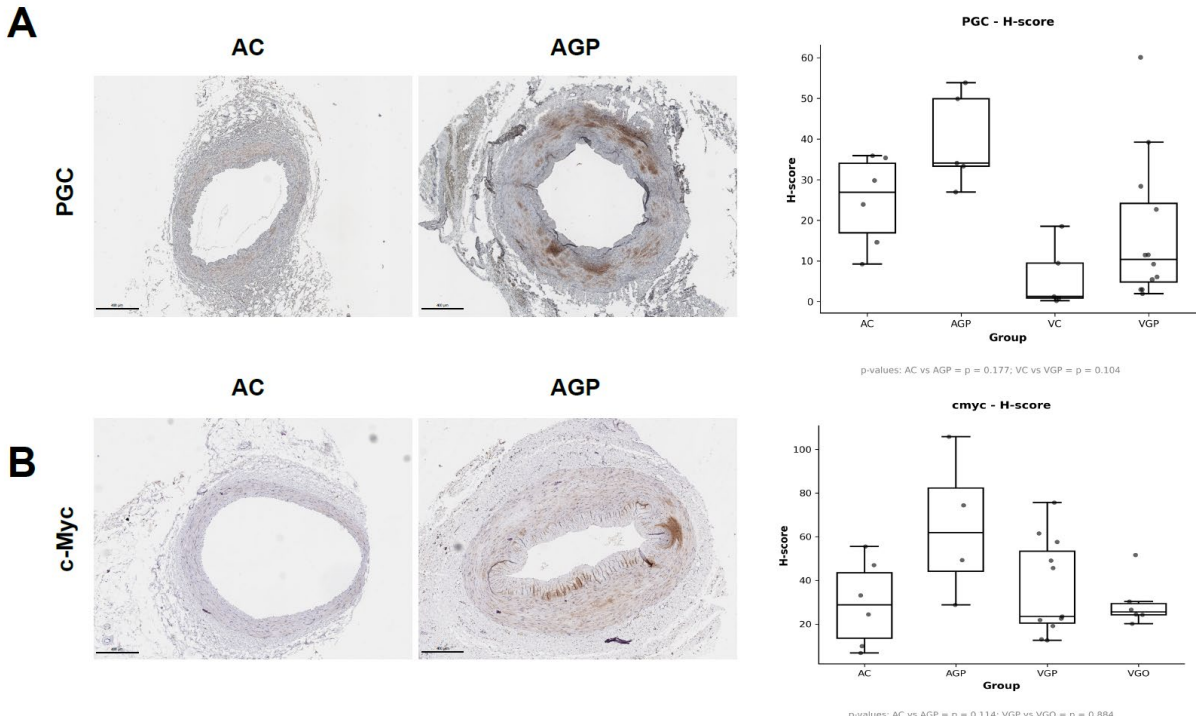

(A) Representative immunohistochemical staining of PGC-1α in native arteries (AC) and patent arterial grafts (AGP) (left), with the corresponding H-score distribution across groups (right). PGC-1α showed an upward trend in both arterial and venous grafts (AGP > AC and VGP > VC), although the differences did not reach statistical significance (AC vs. AGP, P=0.177; VC vs. VGP, P=0.104).

(B) Representative staining and H-score comparison for c-Myc. c-Myc expression was higher in AGP than in AC, but the difference was not statistically significant (P=0.114). No significant differences were observed between VGP and VGO (P=0.884). Scale bars are shown on each image

Supplementary Table 1. Patient characteristics

Patient	Sex	Age at TPL	Index diagnosis	Index operation name	Index operation date	TPL date	Duration from CABG to TPL	ITA graft patency	SV graft patency	ITA blocks	Patent SV blocks	Occluded SV blocks
1	M	62	Severe AS, Ascending aorta aneurysm, NSTEMI with 3VD, LV apical aneurysm (EF 21%)	AVR, ascending aorta replacement, CABG (SV to RIMA (I-graft), SV/LAD & OM & PDA, endoventricular circular patch repair	Feb 2010	Jul 2015	65 months	Patent	Patent	0	3	0
2	M	69	NSTEMI with 3VD, LMD, ICMP (EF 22%), Atrial fibrillation	CABG (ECMO, IABP supported); SV to LIMA (Y-graft); LIMA/LAD, RSVG/D & OM & PLB, LAA obliteration	Aug 2017	Aug 2017	7 days	Patent	Patent	3	2	0
3	M	72	Unstable angina with	redo CABG; SV to ascending aorta, SV/LAD	Jun 2018	Jul 2018	12 days	-	patent	0	2	0

			3VD, ICMP (EF 28%)	(previous CABG; RIMA to LIMA (Y-graft), LIMA/LAD, RIMA/OM, SV/mRCA & PDA at 1997)								
4	M	73	NSTEMI with 3VD, ICMP (EF 35%)	CABG; SV to LIMA (Y-graft), LIMA/LAD, RSVG/D & OM & PLB	Dec 2012	Nov 2019	83 months	Patent	Patent	0	1	0
5	M	49	NSTEMI with 3VD. ICMP (EF 33%)	CABG; SV to LIMA (Y-graft), LIMA/LAD, SV/D & OM & PLB & PDA	Mar 2012	May 2022	123 months	Patent	Patent	2	5	0
6	F	52	Stable angina with 2VD, LV dysfunction (EF 38%)	CABG; SV1 to LITA (I-graft), LITA-SV1/LAD, SV2 to ascending aorta, SV2/D & PLB	Jul 2020	Mar 2023	32 months	Patent	Patent	1	6	0
7	M	66	Stable angina with	Redo CABG; SV to LITA (Y-graft);	Oct 2009	Jun 2022	152 months	Patent	Patent	1	0	2

			2VD, LV dysfunction (EF 35%)	SV/D & LAD & PDA, (previous CABG; RIMA to LIMA (Y-graft), SV to LIMA (Y-graft), LITA/mLAD, SV/dLAD, RITA/OM, in situ RGEA/PDA at 2004)								
8	M	67	3VD	CABG; SV to ascending aorta, LIMA/LAD, SV1/LCX & OM, SV2/RCA	2004	Apr 2023	226 months	Patent	Occluded	6	0	7

AS, aortic stenosis; AVR, aortic valve replacement; CABG, coronary artery bypass grafting; D, diagonal; EF, ejection fraction; IABP, intra-aortic balloon pump; ICMP, ischemic cardiomyopathy; IMA, internal mammary artery; LAA, left atrial appendage; LAD, left anterior descending artery; LCX, left circumflex artery; LIMA, left internal mammary artery; LMD, left main disease; LV, left ventricle; NSTEMI, non-ST elevation myocardial infarction; OM, obtuse marginal; PDA, posterior descending artery; PLB, posterolateral branch; RCA, right coronary artery; RGEA, right gastroepiploic artery; RIMA, right internal mammary artery; SV, saphenous vein; TPL, transplantation; VA

ECMO, venoarterial extracorporeal membrane oxygenator; VD, vessel disease.

Supplementary Table 2. Antibodies used for immunohistochemistry

Antibody	Antibody name / Description	Company	Catalog No.	Host species	Gene name (Full name)
AGT	Anti-Angiotensinogen/AGT Polyclonal antibody	Proteintech	23972-1-AP	Rabbit polyclonal	*AGT* (angiotensinogen; serpin peptidase inhibitor, clade A, member 8)
αSMA	Anti-α-smooth muscle actin	Thermo Fisher Scientific	clone 1A4, MA5-11547	Mouse monoclonal	*ACTA2* (actin alpha 2, smooth muscle)
CD31	Anti-CD31	DAKO	clone JC70A	Mouse monoclonal	*PECAM1* (platelet and endothelial cell adhesion molecule 1)
C-Myc	Anti-C-Myc antibody	Cell Marque	395R-16	Rabbit monoclonal	*MYC* (cellular myelocytomatosis oncogene)
EGFR	Anti-Epidermal Growth Factor Receptor (3C6) Primary Antibody	Ventana	790-2988	Mouse monoclonal	*EGFR* (epidermal growth factor receptor)
eNOS	Anti-endothelial nitric oxide synthase	Cell Signaling Technology	clone 6H2, #5880	Mouse monoclonal	*NOS3* (nitric oxide synthase 3)
IGF1 / IGF2	Anti-IGF1+IGF2 antibody	Abcam	ab9572	Rabbit polyclonal	*IGF1 / IGF2* (insulin-like growth factor 1 and 2)
NKX2.3	Anti-Nkx2.3 Polyclonal Antibody	Invitrogen	PA5-61547	Rabbit polyclonal	*NKX2-3* (NK2 homeobox 3)
NR4A3 (NOR-1)	Anti-NOR-1 antibody	Santa Cruz	sc-393902	Rabbit polyclonal	*NR4A3* (nuclear receptor subfamily 4 group A member 3)
PPARGC1A (PGC-1α)	Anti-PPARGC1A (PGC-1α) antibody	Abcam	ab191838	Rabbit polyclonal	*PPARGC1A* (PPARG coactivator 1 alpha)
PTGES	Prostaglandin E synthase antibody	Novus	NBP1-87852	Rabbit polyclonal	*PTGES* (prostaglandin E synthase)
RETN (Resistin)	Anti-Resistin antibody	Santa Cruz	sc-376336	Mouse monoclonal	*RETN* (resistin)
RUNX2	Anti-RUNX2 antibody	Abcam	ab192256	Rabbit monoclonal	*RUNX2* (RUNX family transcription factor 2)
SRC	Anti-SRC antibody	Abcam	ab109381	Rabbit	*SRC* (SRC proto-oncogene, non-

				monoclonal	receptor tyrosine kinase)
STAT1	Anti-STAT1 antibody	Abcam	ab281999	Mouse monoclonal	*STAT1* (signal transducer and activator of transcription 1)
STAT3 (phospho-Tyr705)	Phospho-STAT3 (Tyr705) antibody	Cell Signaling	#9145	Rabbit monoclonal	*STAT3* (signal transducer and activator of transcription 3)